Characterization and structural basis of a lethal mouse-adapted SARS-CoV-2

Shihui Sun[1†], Hongjing Gu[1†], Lei Cao[2†], Qi Chen[1†], Qing Ye[1†], Guan Yang[3†], Rui-Ting Li[1†], Hang Fan[1†],Yong-Qiang Deng[1], Xiaopeng Song[3], Yini Qi[3], Min Li[1], Jun Lan[2], Rui Feng[2], Yan Guo[1], Na Zhu[4], Si Qin[1], Lei Wang[2], Yi-Fei Zhang[1], Chao Zhou[1], Lingna Zhao[1], Yuehong Chen[1], Meng Shen[1], Yujun Cui[1], Xiao Yang[3], Xinquan Wang[5], Wenjie Tan[4], Hui Wang[1*], Xiangxi Wang[2*], Cheng-Feng Qin[1,6*]

[1]State Key Laboratory of Pathogen and Biosecurity, Beijing Institute of Microbiology and Epidemiology, AMMS, Beijing 100071, China

[2]CAS Key Laboratory of Infection and Immunity, National Laboratory of Macromolecules, Institute of Biophysics, Chinese Academy of Sciences, Beijing 100101, China

[3] State Key Laboratory of Proteomics, Beijing Proteome Research Center, National Center for Protein Sciences (Beijing), Beijing Institute of Lifeomics, Beijing 102206, China

[4] National Institute for Viral Disease Control and Prevention, Chinese Center for Disease Control and Prevention (China CDC), Beijing 102206, China

[5]The Ministry of Education Key Laboratory of Protein Science, Beijing Advanced Innovation Center for Structural Biology, Beijing Frontier Research Center for Biological Structure, Collaborative Innovation Center for Biotherapy, School of Life Sciences, Tsinghua University, Beijing 100084, China

[6] Research Unit of Discovery and Tracing of Natural Focus Diseases, Chinese Academy of Medical Sciences, Beijing 100071, China

*Correspondance to: Cheng-Feng Qin (qincf@bmi.ac.cn), Xiangxi Wang (xiangxi@ibp.ac.cn), or Hui Wang (geno0109@vip.sina.com)

†These authors contributed equally.

Abstract

The ongoing SARS-CoV-2 pandemic has brought an urgent need for animal models to study the pathogenicity of the virus. Herein, we generated and characterized a novel mouse-adapted SARS-CoV-2 strain, named MASCp36, that causes severe acute respiratory symptoms and mortality in standard laboratory mice. Particularly, this model exhibits age and gender related skewed distribution of mortality akin to severe COVID-19, and the 50% lethal dose (LD50) of MASCp36 was 58 PFU in 9-month-old, male BALB/c mice. Deep sequencing identified three amino acid substitutions, N501Y, Q493H, and K417N, subsequently emerged at the receptor binding domain (RBD) of MASCp36, during in vivo passaging. All three mutations in RBD significantly enhanced the binding affinity to its endogenous receptor, mouse ACE2 (mACE2). Cryo-electron microscopy (cryo-EM) analysis of human ACE2 (hACE2) or mACE2 in complex with the RBD of MASCp36 at 3.1 to 3.7 angstrom resolution elucidates molecular basis for the receptor-binding switch driven by specific amino acid substitutions. Interestingly, N501Y and Q493H enhanced the binding affinity to human ACE2 (hACE2); while triple mutations N501Y/Q493H/K417N decreased affinity to hACE2, thus led to the reduced infectivity of MASCp36 to human cells. Our study not only provides a robust platform for studying the pathogenesis of severe COVID-19 and rapid evaluation of coutermeasures against SARS-CoV-2, but also unveils the molecular mechanism for the rapid adaption and evolution of SARS-CoV-2 in human and animals.

One sentence summary

A mouse adapted SARS-CoV-2 strain that harbored specific amino acid substitutions in the RBD of S protein showed 100% mortality in aged, male BALB/c mice.

Introduction

Coronavirus disease 2019 (COVID-19) caused by severe acute respiratory syndrome coronavirus 2 (SARS-CoV-2), has resulted in a public health crisis [1]. The symptoms of COVID-19 are similar to those of SARS-CoV and MERS-CoV infections, ranging from fever, fatigue, dry cough and dyspnea, and mild pneumonia to acute lung injury (ALI) and the acute respiratory distress syndrome (ADS) in severe cases. In fatal cases, multi-organ failures accompanied by a dysregulated immune response have been observed [2,3,4]. Numerous studies have highlighted age and gender related discrepancies in the distribution of COVID-19 cases where the elderly and men tend to have a higher case-fatality ratio when compared to the young and females, suggesting that elderly man are more likely to succumb to COVID-19[5,6].

Similar to SARS-CoV, SARS-CoV-2 belongs to the *Betacoronavirus* genus of the *Coronaviridae* family, and is an enveloped, single stranded positive-sense RNA virus. Human angiotensin-converting enzyme 2 (hACE2), has been demonstrated as the functional receptor for SARS-CoV-2[7,8]. SARS-CoV-2 cannot infect standard laboratory mice due to inefficient interactions between the receptor binding domain (RBD) of Spike (S) protein and mouse ACE2 (mACE2)[9]. So, several hACE2-expressing mouse models such as hACE2 transgenic mice[10], AAV-hACE2 transduced mice[11] and Ad5-hACE2 transduced mice[12] have been developed. Furthermore, mouse adapted strains of SARS-CoV-2 have also been developed *via* either *in vivo* passaging or reverse genetics[13,14,15]. However, most these models cause only mild to moderate lung damage in mice. A small animal model capable of recapitulating the most severe respiratory symptoms and high case fatality ratio of COVID-19 remains of high priority.

In this study, we generated a mouse-adapted strain, MASCp36, from a previous described, MASCp6, by further *in vivo* passaging for additional 30 time in mice[13]. Further characterization demonstrated MASCp36 caused 100% fatality in 9-month-old, male BALB/c mice with severe malfunctions of the respiratory system and multi-organ damage. Combined biochemical assay, viral genome sequencing, and cryo-EM analysis clearly demonstrated the critical role of the progressively emerged amino acid mutations in the RBD of the mouse-adapted strains at different passages.

Results

Generation of a lethal mouse-adapted strain of SARS-CoV-2.

In our previous study, we generated a mouse-adapted strain of SARS-CoV-2 (MASCp6) by 6 serial passages of a SARS-CoV-2 clinical isolate in the lung of BALB/c mice, which caused moderate lung damage in mice. Herein, we further serially passaged for additional 30 times to generate a more virulent mouse-adapted strain, and the resulting SARS-CoV-2 at passage 36 (named as MASCp36) was used for stock preparation and titration.

To characterize the pathogenicity of MASCp36 to standard laboratory mice, groups of BALB/c mice at different age and sex were subjected to intranasal injection of varying doses of MASCp36. Strikingly, survival curve analysis showed that 9-month-old mice are highly susceptible to MASCp36 challenge, and the infected animals succumbed to MASCp36 challenge in a dose dependent manner. What's more, male mice were more susceptible to MASCp36 in comparison to female ones, and the 50% lethal dose (LD50) was calculated to 58 PFU (male) and 690 PFU (female), respectively (Fig. 1a, b). All 9-month-old mice challenged with high doses (1,200 or 12,000 PFU) of MASCp36 developed typical respiratory symptoms and exhibited features like ruffled fur, hunched back, and reduced activity. Of particular note, tachypnea was common in all moribund animals. Additionally, this unique gender-dependent mortality was also recorded in 9-month-old C57BL/6 mice challenged with MASCp36 (Supplementary Fig. 1). Interestingly, 8-week-old mice, either male or female, were resistant to MASCp36 challenge, and only 1 animal that received 12,000 PFU of MASCp36 challenge died during the observation period (Fig. 1c-d). Thus, the newly-developed MASCp36 was sufficient to cause mortality in BALB/c or C57BL/6 mice in an age and gender skewed manner.

We further characterized the *in vivo* replication dynamics and tissue distribution of MASCp36 in mice. The results from qRT-PCR showed that high levels of SARS-CoV-2 subgenomic RNAs were persistent in the lung and tracheas till 4 day post infection (dpi) in 9-month-old mice (Fig. 1e). Interestingly, the 8-week-old mice sustained a similar tissue distribution as the 9-month-old ones upon MASCp36

challenge, and lung and tracheas represented the major tissues supporting viral replication (Fig. 1f). Consistent with the sgRNA levels, infectious SARS-CoV-2 could be recovered in the lung homogenate from 9-month-old and 8-week-old mice that received MASCp36 challenge (Fig.1g, h). Multiplex immunofluorescence staining showed that large amount of SARS-CoV-2 N protein positive signals were detected in lung sections from the MASCp36-infected mice (Fig. 2a, b), and co-localization with the SPC$^+$ alveolar type 2 (AT2) cells and CC10$^+$ club cells, as well as the ACE2$^+$ club cells, were shown (Fig.2a); while few FOXJ1$^+$ ciliated cells and PDPN$^+$ alveolar type 1 (AT1) cells were infected with SARS-CoV-2 (Fig. 2a). More importantly, despite more SPC$^+$AT2 cells were detected in the lung of younger mice, SARS-CoV-2-infected cells were more abundant in the lung from 9-month-old mice than those from the 8-week-old animals (Fig. 2b). In fact, the ratio of ACE2$^+$ AT2 cells in the un-infected 9-month-old mice was much higher than that in the un-infected 8-week-old mice (Fig. 2c), which supported the observed age-skewed susceptivity to SARS-CoV-2.

MASCp36 causes multiple organs damage in mice.

To further characterize the pathological outcome in MASCp36-infected mice, lung tissues were collected at 4 dpi and subjected to histopathological and immunostaining analysis. Naked eye observation recorded severe lung injury characterized with bilateral cardinal red appearance and sticky mucus in lungs when compared with that from the un-infected control animals (Fig. 3a). According to the metrics of acute lung injury (ALI) laid out by the American Thoracic Society (ATS)[16], MASCp36 infection induced necrotizing pneumonia and extensive diffuse alveolar damages (DAD) on 4 dpi. The microscopic observation showed large quantities of desquamative epithelial cells in bronchiole tubes (yellow arrow) and a large area of necrotic alveoli epithelial cells, fused alveoli walls with inflammatory cells infiltration especially neutrophils in alveolar septae or alveolar airspace, serious edema around vessels (cyan arrow) and scattered hemorrhage (blue arrow) (Fig. 3a). In addition, foamy cells, polykaryocytes, fibrin cluster deposition, and hyaline membrane formation were common in the MASCp36 infected animals (Fig. 3b), indicative of acute lung injury, which is well characterized in severe COVID-19 patients[4]. Besides, the formation of typical viral inclusion bodies were also observed (Fig. 3b). Additionally, we also observed the lung pathology in 9-month-old male mice infected with a lower dose (120 PFU) of

MASCp36 at 7 dpi. As shown in Fig. 3c, lung fibrosis was observed in the MASCp36-infected mice as evidenced by the depositions of collagen in pulmonary artery wall and thickened alveoli. Meanwhile, an increased proliferation of alveolar mesenchymal cells was also observed in MASCp36-infected mice (Supplementary Fig. 2).

Apart from the lung damage, spleen damage was also observed in MASCp36-infected mice, which was characterized by atrophic splenic corpuscle, splenic cells necrosis and hemorrhage in red pulp (green arrow) (Fig. 4a). Multiplex immunofluorescence staining showed a striking loss of germinal centers in the spleen as suggested by the reduction in CD19$^+$ B and CD3$^+$ T cell counts as well as diminished ICOS$^+$ follicular helper T cells (Fig. 4b). Similar observations have been well described in severe COVID-19 patients[17]. In addition, renal tubular damage with casts in renal tubules, as well as breakdown of CD31$^+$ glomerular capillary epithelium and PDPN$^+$ basement membrane were also observed in kidney (Fig. 4c,d). Similar splenic lesion and kidney damage were also reported in cases with postmortem examinations of deceased COVID-19 patients [18, 19].

MASCp36 induces age- and gender-specific response in mice.

To characterize the host response to MASCp36 infection in BALB/c mice at different age and gender, RNA-Seq analysis were performed using lung homogenates collected at 1 and 4 dpi. Upon MASCp36 infection, large numbers of genes were readily regulated in both 8-week-old and 9-month-old mice at 1 dpi (Fig. 5a). In the MASCp36-infected 9-month-old mice, 16 of the top 20 up-regulated genes were Interferon simulated genes (ISGs) and cytokines, including Cxcl10, Mx1, Gbp7, Mx2, Ifi44, Oasl2, Itgp, Gbp9, Isg15, Ifit1, Gbp4, Irgm2, Irf7, Ifit2, Stat2; while in the 8-week-old mice, only Ifit3, Mx2, Trim34b, Ifi44l and Rtp4 were related to antiviral immunity. At 4 dpi, the 9-month-old mice exhibited more dramatic response with a total of 2762 up-regulated genes and 2363 down-regulated genes. And cytokines Il6 and Ccl2 were among the top 20 up-regulated genes at 4 dpi; while ISGs including Mx1, Ifit1, Ifit3, Irf7, Dhx58 and Ifi44 were in the MASCp36-infected 8-week-old mice (Fig. 5a). Gene Ontology (GO) enrichment analyses showed that MASCp36 infection induced strong transcription of genes related to antiviral response, inflammatory, cytokine production and cell death in both 8-week-old and 9-month-old

mice infected with MASCp36 (Fig. 5b). Strikingly, the induction of "cytokine production", "leukocyte activation", "inflammatory response", "interferon-gama production" and "positive regulation of cell death" was much quicker and stronger in the older mice. Of particular note, a large number of cytokines and chemokines transcription were up-regulated in response to MASCp36 in 9-month-old mice, while less and smaller up-regulation of cytokines and chemokines were observed in 8-week-old mice. Ccl2, Ccl7, Il6, Cxcl10 and Cxcl11 were the most significant up-regulated genes in the MASCp36-infected 9-month-old mice (Fig. 5c). Meanwhile, Luminex analysis also detected obvious elevated cytokine and chemokine production, including IL6, CCL7, CCL12, CXCL10, CXCL16, CCL3, CXCL1, CXCL13, in the lung homogenates from the MASCp36 infected mice (Fig. 5d and Supplementary Fig. 3). Strikingly, we found many genes involved in "cilium movement" were significantly stimulated at 1 and 4 dpi in the younger mice, while only a small number of genes were upregulated in the older mice at 4 dpi (Fig 5e).

Additionally, immunofluorescence staining of lung sections also indicated MASCp36 infection caused more extensive cell death and AT2 loss in the 9-month-old mice (Fig. 6a). Interestingly, less CD68^{+} macrophages and Ly-6G^{+} neutrophils were detected in 9-month-old mice than that in young mice 1 dpi (Fig. 6b), and reversed on 4 dpi. Of note, although the inflammatory cell infiltration was lagged on day 1 in 9-month-old mice, it elevated and sustained a high level until 4 days. However, the response was rapid and short-lived in young mice. The results indicated that the lagged and sustained immune response to viral infection may be related to the lung damage and contribute to the more severe outcomes in 9-month-old mice.

Furthermore, to understand the gender-skewed mortality in mice, we also compared the different gene expression in lungs of male and female mice. First of all, we confirmed that 1075 genes were significantly highly expressed in female mice (Supplementary Fig. 4a) in total of 1308 DEGs, and the genes enriched in "Cilium movement", "Immunoglobin production", "Adaptive immune responses" and "Cellular response to interferon-beta" GO terms, which coincided with previous studies[20]. After infection, both the antiviral response and inflammatory response were stronger elevated in female mice when compared to the male especially on 1dpi (Supplementary Fig. 4 b, c) .

H014 confers full protection in lethal MASCp36 model.

To further test the utility of this MASCp36-based mouse model for evaluation of countermeasures, H014, a known human monoclonal antibody (mAb) targeting the RBD of SARS-CoV-2[21], was examined for its ability to prevent mortality caused by MASCp36. Administration of a single dose of H014 (50 mg/kg) resulted in 100% survival (Fig. 7a) and complete clearance of virus from the lungs of infected mice (Fig. 7 b , c). By contrast, all animals that received a control isotype mAb treatment showed high levels of viral replication in lungs and eventually died with respiratory diseases within 5 days (Fig. 7a-c). Multiplex immunofluorescence staining demonstrated H014 treatment completely protected animals from viral infection and no viral antigen was detected at 4 dpi, while significant AT2 loss and neutrophil infiltration were seen in the mice treated with isotype mAb (Fig. 7c). H&E staining also confirmed that H014-treatment dramatically prevented the MASCp36-induced lung damage characterized by fused alveoli walls, desquamative epithelial cells, severe edema and scattered hemorrhage (Fig. 7d). These data perfectly match the results from hACE2 humanized mice[21], highlighting the potential of MASCp36-based models in evaluating the *in vivo* therapeutic efficacy.

Adaptive mutations responsible for the enhanced binding affinity to ACE2.

To deduce the genetic basis for the lethal phenotype of MASCp36, deep sequencing was performed to identify the mutations emerged during the *in vivo* passaging history. Sequence comparisons of the WT strain and mouse-adapted strains at different passages (6, 15, 25, 30, and 36) revealed a process of gradual accumulation of amino acid substitutions (Fig. 8a). Besides the four mutations (L37F, P84S, N501Y, and D128Y) identified in MASCp6, MASCp36 acquires additional 8 amino acid substitutions, including I1258V, H470Y, S301L, A128V, S8F, K417N, Q493H, and R32C in the NSP3, NSP4, NSP5, NSP6, NSP7, S and N (Fig.8a). Specially, single (N501Y), double (Q493H, N501Y) and triple (K417N, Q493H, N501Y) mutations in the RBD were identified in MASCp6, MASCp25 and MASCp36, respectively (Fig. 8b). To clarify the potential role of these mutations, the RBD of these different adaptive strains were expressed in HEK Expi 293F cells, and their binding affinities to mACE2 were determined by surface plasmon resonance (SPR). As expected, the

RBD of WT SARS-CoV-2 presented no detectable binding, but RBDs from different passages of mouse-adapted strains (RBD$_{MASCp6}$, RBD$_{MASCp25}$ and RBD$_{MASCp36}$) gain gradually enhanced binding abilities to mACE2 with affinities ranging from ~500 μM to 2 μM (Fig. 8c). Meanwhile, we also compared the binding characterization of these RBD mutants and hACE2. As shown in Fig. 8d, all three RBD mutants could bind to hACE2 with affinities at nanomole (ranging from 500 nM to 20 nM). Interestingly, compared to RBD$_{MACSp6}$ with a mutation of N501Y, RBD$_{MACSp25}$, which contains an extra Q493H substitution, showed an enhanced binding affinity to hACE2. However, the third substitution of K417N significantly reduced binding activity of RBD$_{MACSp36}$ to hACE2, rendering a lower affinity than that of RBD$_{WT}$. Collectively, these results demonstrated MASCp36 retained the high binding affinity to hACE2.

Furthermore, to confirm whether the mouse-adapted strain MASCp6 retained the infectivity to human cells, primary human airway epithelia (HAE) culture was infected with MASCp36 and WT SARS-CoV-2, respectively. Although both MASCp36 retained the infectivity to HAE (Fig. 9a), the progeny viral RNA loads of MASCp36 were much lower than that of WT SARS-CoV-2 (Fig. 9b), which was consistent to the binding affinity assay.

Structural basis for the enhanced virulence of MASCp36.

Finally, to elucidate the molecular basis for the gradual changes in specificity of MASCp36, structural investigations of the mACE2 in complex with RBD$_{MASCp25}$ or RBD$_{MASCp36}$ were carried out. Two non-competing Fab fragments that recognize the RBD beyond the mACE2 binding sites were used to increase the molecular weight of this complex for pursuing an atomic resolution by cryo-EM reconstruction (Supplementary Fig. 5-8). Interestingly, cryo-EM characterization of the mACE2 in complex with RBD$_{MASCp25}$ revealed that the complex adopts three distinct conformational states, corresponding to tight binding (state 1), loose binding (state 2) and no binding modes (state 3) (Supplementary Fig. 9), indicative of a quick association and quick dissociation interaction manner between the mACE2 and RBD$_{MASCp25}$. However, only the tight binding conformation was observed in the mACE2-RBD$_{MASCp36}$ complex structure, reflecting a more stable/mature binding mode for the RBD$_{MASCp36}$ to mACE2, akin to that of the RBD$_{WT}$ and hACE2. We

determined asymmetric cryo-EM reconstructions of the mACE2-RBD$_{MASCp36}$ complex at 3.7 Å and three states of the mACE2-RBD$_{MASCp25}$ complex at 4.4 to 8.2 Å (Supplementary Fig.6, Supplementary Fig.7, Supplementary Fig.9, Supplementary Fig.10 and Supplementary table 1). The map quality around the mACE2-RBD$_{MASCp36}$ interface was of sufficient quality for a reliable analysis of the interactions (Fig. 10a, Supplementary Fig. 7 and Supplementary table 2).

The overall structure of the mACE2-RBD$_{MASCp36}$ complex resembles that of the RBD$_{WT}$-hACE2 complex with a root mean square deviation of 1.0 Å (Supplementary Fig.8). The RBD$_{MASCp36}$ recognizes the helices (α1 and α2) located at the apical region of the mACE2 *via* its receptor binding motif (RBM) (Fig. 10a-c). The interaction area on the mACE2 could be primarily divided into three patches (PI, PII and PIII), involving extensive hydrophilic and hydrophobic interactions with three regions separately clustered by three adaptation-mediated mutated residues (K417N, corresponding to Clus1; Q493H, corresponding to Clus2; and N501Y, corresponding Clus3) in the RBM (Fig. 10 c-e). Coincidentally, a number of amino acid substitutions, such as Q493K, Q498Y and P499T, in the RBM identified in other reported mouse-adapted SARS-CoV-2 isolates[14, 15, 22] were included either in the Clus2 or Clus3, underlining the putative determinants for cross-transmission (Fig. 10 d,e). An extra Clus1 is further accumulated in the MASCp36 to gain utmost binding activity and infection efficacy (Fig. 10 d,e). The extensive hydrophobic interactions in Clus3 constructed by Y501 (or Y498 or H498 in other mouse-adapted SARS-CoV-2 isolates), Y505 in the RBD$_{MASCp36}$ and Y41, H353 in the mACE2, hydrogen bonds in Clus2 formed H493 (K493 in other mouse-adapted strain) in the RBD$_{MASCp36}$ and N31, E35 in the mACE2 and hydrophilic contacts constituted by N417 in the RBD$_{MASCp36}$ and N30, Q34 in the mACE2 contribute to the tight binding of the MASCp36 to mACE2. Contrarily, structural superimposition of the RBD$_{WT}$ over the mACE2-RBD$_{MASCp36}$ complex reveals the loss of these interactions, leading to the inability of the RBD$_{WT}$ to bind mACE2 (Fig. 9e).

Meanwhile, the atomic structures of hACE2 in complex with RBD$_{MACSp6}$, RBD$_{MACSp25}$ or RBD$_{MACSp36}$ were also solved at 3.1 to 3.7 Å (Supplementary Fig.11, Supplementary table 3). The same as RBD$_{MACSp36}$-mACE2 complex, the interaction region could be divided into three patches, the three adaption-mutated residues

(K417N, located at PI; Q493H, located at PII; and N501Y, located at PIII) were located at the three patches, respectively (Fig 10.f). The extensive hydrophobic interactions in PIII were constructed by Y501, T500 in the RBD and Y41, L45 in the hACE2, salt bridge interactions in PII were formed by H493 in the RBD and E35 in the hACE2. However, in PI, the substitution of K with N at residue 417 in RBD$_{MACSp36}$ loses the salt bridge interaction, which would be formed by K417 in the RBD$_{WT}$ and D30 in the hACE2, structurally explaining the reduced binding affinity of RBD$_{MACSp36}$ to hACE2. Overall, these analysis pinpoints key structure-infectivity correlates, unveiling the molecular basis for host adaptation-mediated evolution of SARS-CoV-2.

Discussion

Clinically, the severe COVID-19 disease onset might result in death due to massive alveolar damage and progressive respiratory failure [23, 24]. However, most animal models previously described recaptulated the mild to moderate clinical symptoms of COVID-19. The MASCp36-based mouse model described here recapitulated most spectrums of seriously ill COVID-19 patients caused by SARS-CoV-2 infection, such as pulmonary oedema, fibrin plugs in alveolar, hyaline membrane, and scattered hemorrhage[25, 26]. The complicated immunopathological phenomena observed in severe COVID-19 patients, such as massive macrophages and neutrophils infiltration, and excessively increased proinflammatory cytokines such as IL-6, were also observed in this MASCp36 infected mouse model. Herein, 9-month-old, male BALB/c mice infected with MASCp36 developed DAD, as well as comprehensive vasculature damage (Fig.3). Importantly, thick fluid in pericardial cavity, hemorrhage and severe edema with less lymphocyte-cuff were observed in lung tissue, resembling clinical manifestations of severe COVID-19 [4].

Lung fibrosis and regeneration were also observed in this model which is the signs of fibrosis in clinic. Although SARS-CoV-2 viral antigen has been detected in kidney of post-mortem specimens [27], no viral antigen or viral RNA were detected in our model (Fig.1e,f). So in this MASCp36 infected mouse model, the kidney injury may arise due to secondary endothelial injury leading to proteinuria[28]. In addition,

although SARS-CoV-2 has also been implicated to have neurotropic potential in COVID-19 [29], we did not find typical characteristics of viral encephalitis in this model. Importantly, the imbalanced immune response with high-levels of proinflammatory cytokines, increased neutrophils and decreased lymphocytes, which were in line with SARS-CoV and MERS-CoV infections [30], playing a major role in the pathogenesis of COVID-19 [31], were also observed in this model.

The skewed age distribution of COVID-19 disease was reproduced in the MASCp36 infected mouse model where more severe symptoms were observed in 9-month-old mice when compared to young mice. Different from H1N1 pandemic[32], COVID-19 appears to have a mild effect on populations under 30 years, and the elderly are more likely to progress to severe disease and are admitted to intensive care unit (ICU) worldwide[33]. ACE2, the functional receptor of SARS-CoV-2, expressed increasingly in the lungs with age, which might provide an explanation to the higher disease severity observed in older patients with COVID-19[34]. More importantly, the host immune response may determine the outcome of the disease. Our immune system is composed of innate immunity and adaptive immunity. The innate immunity comprises of the first line of defense against pathogens and is acute as well as short lived. However, aging is linked with insufficient, prolonged and chronic activation of innate immunity associated with low-grade and systemic increases in inflammation (inflamm-aging) which can be detrimental for the body[35]. The delicate co-operation and balance are interrupted by the chronic activation of innate immunity and declined adaptive immune responses with increasing age in COVID-19[36]. In the MASCp36 infected mouse model, the young mice presented acute inflammatory response with more innate immune cells infiltration on day 1, while lagged and sustained immune response in 9-month-old mice. After further analyzing the RNA-Seq results, we observed robust innate immune response at 1dpi in 9-month-old mice. While we found that T cell activation in 9-month-old mice was not as strong as in 8-week-old mice at 4 dpi. Meanwhile, we found genes involved in "cilium movement" were significantly stimulated at 1 and 4dpi in 8-week-old male mice. While much less genes related to cilium movement were upregulated in 9-month-old male mice till 4 dpi. Previous studies show that mucociliary clearance is an important defense mechanism in the respiratory tract that requires coordinated ciliary activity and proper mucus production to propel airway surface liquids that traps pathogens and pollutants,

permitting their clearance from the lungs[37, 38, 39]. A recent study on ACE2 shows the receptor protein robustly localizes within the motile cilia of airway epithelial cells, which likely represents the initial or early subcellular site of SARS-CoV-2 viral entry during host respiratory transmission[40]. So, we concluded that stimulation of cilium movement may be benefit to young mice to clear virus at the early stage of infection, and over-stimulated innate immune response and reduced adaptive immune response may lead to higher mortality in male 9-month-old mice. The different immune response in mice model may be vital in limiting virus replication at early times and contribute to different outcome on day 4 in young or 9-month-old mice.

In addition to the age-related skewed distribution of COVID-19, gender-related differences in distribution of COVID-19 disease is also recapitulated in this MASCp36 infected mouse model with increased susceptibility and enhanced pathogenicity observed in male mice when compared to their female counterparts. Biological sex is an important determinant of COVID-19 disease severity[41]. In China, the death rate among confirmed cases is 2.8% for women and 4.7% for men [34]. In Italy, half of the confirmed COVID-19 cases are men which account for 65% of all deaths [42]. This pattern is generally consistent around the world. The skewed distribution of COVID-19 suggests that physiological differences between male and female may cause differential response to infection. So the hypothesis that females display reduced susceptibility to viral infections may be due to the stronger immune responses they mount than males[43]. In this study, based on the RNA-Seq results, we also found that female 9-month-old mice show higher intrinsic expression level of immune response related genes than male 9-month-old mice. Stronger immune response was also observed in female 9-month-old mice after infection. It has been studied that androgens may lower and estrogens may enhance several aspects of host immunity. Channappanavar etal.[44] had studied that estrogen receptor signaling is critical for protection in females against SARS-CoV infection. So, we speculated here that estrogen may also play an important role in the protection against MASCp36 infection in female mouse model. In addition, androgens facilitate and estrogens suppress lymphocyte apoptosis. Furthermore, genes on the X chromosome important for regulating immune functions, and androgens may suppress the expression of disease resistance genes such as the immunoglobulin superfamily [45]. In the MASCp36 infected mouse model, we found out that it presented higher mortality of the male

than the female infected with the same dose of virus, indicating the successful recapitulation of COVID-19 and also its potential application in the study of the pathogenesis of the disease.

A total of 12 amino acid mutations were identified in the genome of MASCp36 in comparison with WT SARS-CoV-2 strain. The sequentially acquired triple substitutions N501Y/Q493H/K417N in S protein of MASCp36 increased their affinities to mACE2, thus contributed to enhanced infectivity and lethal phenotype mice. Interestingly, MASCp36 showed decreased affinity to hACE2 (Fig.8d) as well as decreased infectivity to primary human airway epithelia cells (Fig. 9) in comparison with WT SARS-CoV-2. These experimental observations were further verified by structural analysis in which MASCp36 loses the key salt bridge interaction with hACE2 when compared to WT SARS-CoV-2 (Fig10.f). More importantly, Cryo-EM structures of both hACE2 and mACE2 in complex with $RBD_{MASCp25}$ and $RBD_{MASCp36}$ define preciously the atomic determinants of the receptor-binding switch: N501Y/Q493H/K417N in MASCp36 formed tight interactions with mACE2 in three patches, respectively, while K417N reduced interaction with hACE2. Thus, MASCp36 showed enhanced virulence in mice whereas decreased infectivity to human cells.

In addition, there are 9 amino acid substitutions outside the S protein of MASCp36 (Fig. 8a). Notably, R32C and D128Y in the N protein deserves special attention. The D128Y mutation in N protein has been well recorded in human variants from D128Y[46] . A recent report demonstrated acts as an antagonist of interferon (IFN) and viral encoded repressor of RNA interference[47]. Previous studies also reported N protein help package encapsidated genome into virions via binding Nps3[48]. Also, mutations were note in Nsp3 and Nsp5 which play role in blocking host innate immune response, promoting cytokine expression and inhibiting IFN signaling. Further studies will focus on the influence of virus changes to host innate immunity in mice[49]. Recently, Shi and colleagues found that SARS-CoV-2 nsp1 and nsp6 suppress IFN-I signaling which provides insights on viral evasion and its potential impact on viral transmission and pathogenesis[50]. Whatever, multiple amino acid substitution might contribute to the enhanced virulence phenotype, independently or synergistically. At present, we cannot rule out the contribution of these mutations, and further validation with reverse genetic tools will help understand the biological

function of each single mutation[51].

There is another interesting point that deserve concerns. These adaptive mutations emerged during mouse passage, however many of them have been documend in SARS-CoV-2 variants during human transmission. For example, the 501Y.V1 variant firstly detected in the United Kingdom (UK) contained the unique N501Y mutation in RBD[52], and more recent SARS-CoV-2 variants (501Y.V2 and 501Y.V2) contained both N501Y and K417N substitutions in S protein[53]. Except for N501Y and K417N, several other amino acid substitutions in MASCp36 were also found in human variants, including L37F in nsp6 and D128Y in N protein[46, 54]. The coincidental emergence of the same mutations during mice passaging and COVID-19 epidemics highlight the importance of these mutations during host adaption.

In conclusion, our MASCp36 mouse model exhibited symptoms of DAD and acute lung injury in both laboratory standard BALB/c and C57BL/6 rodent model, which largely simulated COVID-19 severe disease. And the age and gender-dependent mortality well reproduced the clinical findings of human COVID-19. This novel model will be of high value for studying the pathogenesis of COVID-19 with genetic modified mice and for the rapid efficacy tests of potent countermeasures against SARS-CoV-2.

Materials and Methods

Ethics statement. All procedures involving infectious virus were conducted in Biosafety Level 3 laboratory (BSL-3) and approved by the Animal Experiment Committee of Laboratory Animal Center, Beijing Institute of Microbiology and Epidemiology (approval number: IACUC-DWZX-2020-002).

Virus and mice. Mouse adapted strain of SARS-CoV-2 (MASCp6) was developed from a clinical SARS-CoV-2 isolate in our previous study[13]. Additional serial passage of 30 times was performed as previously described[13] . BALB/c and C57BL/6 mice were purchased from Beijing HFK Bioscience Co., LTD and Beijing Vitalriver Laboratory Animal Technology Co. Ltd. The virus stock of MASCp36 was amplified and titrated by standard plaque forming assay on Vero cells.

Measurement of viral sgRNA. Tissue homogenates were clarified by centrifugation at 6,000 rpm for 6 min, and the supernatants were transferred to a new EP tube. RNA was extracted using the QIAamp Viral RNA Mini Kit (Giagen) according to the manufacturer's protocol[13]. sgRNA quantification in each sample was performed by quantitative reverse transcription PCR (RT-qPCR) targeting the E subgenomic mRNA of SARS-CoV-2. RT-qPCR was performed using One Step PrimeScript RT-PCR Kit (Takara, Japan) with the following primers and probes [55]: sgRNA-Leader (5'-CGATCTCTTGTAGATCTGTTCTC-3'); sgRNA-Reverse (5'-ATATTGCAGCAGTACGCACACA-3'); and sgRNA-Probe (5'-ACACTAGCCATCCTTACTGCGCTTCG-3').

Deep sequencing. Total RNA was extracted after each passage using High Pure Viral RNA Kit (Roche, Switzerland), and the purified viral RNA was used for library construction using Ion Total RNA-Seq kit V2 (Thermo Fisher, USA). The library was sequenced on an Ion Torrent S5Plus sequencer (Thermo Fisher, USA). Sequences were assembled and analyzed with CLC Genomic Workbench (Qiagen, Germany). All reads were mapped to SARS-CoV-2 reference genome (Wuhan-Hu-1, GenBank accession number MN908947). The consensus sequence was extracted. Single nucleotide variations with variation proportion above 1% were called using this software.

Mouse virulence study. Female and male 6 weeks- and 9 months BALB/c and C57BL/6 mice were maintained in a pathogen-free facility and housed in cages containing sterilized feed and drinking water. Following intraperitoneal (i.p.) anesthetization with sodium pentobarbital, mice were intranasally (i.n.) inoculated with varying doses of MASCp36 or the same volume of PBS for mock infection. Four mice of each group were sacrificed on days 1 and 4 after infection for lung damage study and sgRNA quantification. Clinical manifestation and survival were recorded for 14 days.

Histopathological analysis. Lung, heart, liver, spleen, kidney, brain, intestine and trachea tissues were collected 4 days post infection with MASCp36, and paraffin-embedded in accordance with standard procedure. Sections at 4 μm thickness were stained with hematoxylin and eosin (H&E) and examined by light microscopy and analyzed by two experienced experimental pathologists.

Multiplex immunofluorescent assay. The multiplex immunofluorescence assay was conducted as previously described[13]. Briefly, the retrieved sections were incubated with primary antibody for 2 h followed by detection using the HRP-conjugated secondary antibody and TSA-dendron-fluorophores (NEON 7-color Allround Discovery Kit for FFPE, Histova Biotechnology, NEFP750). Afterwards, the primary and secondary antibodies were thoroughly eliminated by heating the slides in retrieval/elution buffer (Abcracker®, Histova Biotechnology, ABCFR5L) for 10 sec at 95°C using microwave. In a serial fashion, each antigen was labeled by distinct fluorophores. Multiplex antibody panels applied in this study include: ACE2 (Abcam, ab108252, 1:200); SARS-CoV-2 N protein (Sinobiological, 40143-R004, 1:2000); CC10 (Millipore, 07-623, 1:500), FOXJ1 (Abcam, ab235445, 1:1000), SPC (Abcam, ab211326, 1:500), Cleaved caspase-3 (CST, 9664, 1:300); Ly-6G (CST, 87048, 1:400); CD68 (CST, 97778, 1:300); CD3 (CST, 78588, 1:300); CD19 (Abcam, ab245235, 1:800); ICOS (Abcam, ab224644, 1:200); CD31 (CST, 77699, 1:300). After all the antibodies were detected sequentially, the slides were imaged using the confocal laser scanning microscopy platform Zeiss LSM880. Some data were further processed and statistically analyzed using Bitplane Imaris software (Bitplane AG, Zurich, Switzerland).

Cytokine and chemokines analysis. Cytokines and chemokines in mouse lung homogenates were measured using a Bio-Plex Pro Mouse Cytokine Grp I Panel 31-Plex (Bio-Rad, USA) according to the manufacturer's protocol. The data were collected on Luminex 200 and analyzed by Luminex PONENT (Thermo Fisher, USA).

RNA sequencing and Bioinformatic analyses. Lung homogenates from MASCp36-infected mice (male, 8-week-old; male, 9-month-old; female, 9-month-old) or mock treated mice were processed as previously described[13] and subjected to RNA-Seq. Total RNA from lung tissue were extracted using TRIzol (Invitrogen, USA) and treated with DNase I (NEB, USA). Sequencing libraries were generated using NEBNext® UltraTM RNA Library Prep Kit for Illumina® (NEB, USA) following the manufacturer's recommendations and index codes were added to attribute sequences to each sample. The clustering of the index-coded samples was performed on a cBot cluster generation system using HiSeq PE Cluster Kit v4-cBot-HS (Illumina) according to the manufacturer's instructions. After cluster generation, the libraries

were sequenced on Illumina Novaseq6000 platform and 150 bp paired-end reads were generated. After sequencing, perl script was used to filter the original data (Raw Data) to clean reads by removing contaminated reads for adapters and low-quality reads. Clean reads were aligned to the mouse genome (Mus_musculus GRCm38.99) using Hisat2 v2.1.0. The number of reads mapped to each gene in each sample was counted by HTSeq v0.6.0 and TPM (Transcripts Per Kilobase of exon model per Million mapped reads) was then calculated to estimate the expression level of genes in each sample. DESeq2 v1.6.3 was used for differential gene expression analysis. Genes with padj≤0.05 and |Log2FC| > 1 were identified as differentially expressed genes (DEGs). DEGs were used as query to search for enriched biological processes (Gene ontology BP) using Metascape. Heatmaps of gene expression levels were constructed using heatmap package in R (https://cran.rstudio.com/web/packages/pheatmap/index.html). Dot plots and volcano plots were constructed using ggplot2 (https://ggplot2.tidyverse.org/) package in R.

In vivo efficacy assay with MASCp36 model. Group of 9-month male BALB/c mice were inoculated intranasally with 40 μL MASCp36 (1, 200 PFU) and intraperitoneally administered 200 µL of H014 (50 mg/kg) at 24 hours before and after MASCp36 infection. The same volume of an isotype antibody was administrated as control. On day 4 post infection, 3 mice in each group were sacrificed and lung tissues were prepared for pathology analysis and sgRNA quantification. The other 6 mice in each group were monitored for survival for 14 days.

Protein expression and purification. The cloning and production of SARS-CoV-2 RBD (residues 319-541, GenBank: MN_908947.3), RBD mutants (RBD$_{MACSp25}$: Q493H, N501Y; RBD$_{MACSp}$36: K417N, Q493H, N501Y) hACE2 (residues 19-624, GenBank: NM_021804.3) and mACE2 (residues 19-739, GenBank: NM_001130513.1) were synthesized and subcloned into the mammalian expression vector pCAGGS with a C-terminal 2×StrepTag to facilitate protein purification. Briefly, RBD$_{WT}$, RBD$_{MACSp25}$, RBD$_{MACSp36}$, hACE2 and mACE2 were expressed by transient transfection of HEK Expi 293F cells (Gibco, Thermo Fisher) using Polyethylenimine Max Mw 40,000 (polysciences). The target protein was purified from clarified cell supernatants 3 days post-transfection using StrepTactin resin (IBA). The resulting protein samples were further purified by size-exclusion chromatography

using a Superdex 75 10/300 column (GE Healthcare) or a Superdex 200 10/300 Increase column (GE Healthcare) in 20mM HEPES, 200 mM NaCl, pH 7.0.

To purify the final quaternary complex ($RBD_{MACSp25}$/$RBD_{MACSp36}$-Fab_{B8}-Fab_{D14}-mACE2), firstly, the ternary complex ($RBD_{MACSp25}$/$RBD_{MACSp36}$ -Fab_{B8}-Fab_{D14}) was assembled. $RBD_{MACSp25}$ or $RBD_{MACSp36}$ was mixed with Fab_{B8} and Fab_{D14} at the ratio of 1 : 1.2 : 1.2, incubated for 30 min on ice. The mixture was then subjected to gel filtration chromatography. Fractions containing the ternary complex ($RBD_{MACSp25}$/$RBD_{MACSp36}$-Fab_{B8}-Fab_{D14}) were pooled and concentrated. Then mACE2 was mixed with the ternary complex ($RBD_{MACSp25}$/$RBD_{MACSp36}$-Fab_{B8}-Fab_{D14}) at the ratio of 1 : 1.2 and incubated for 60 min on ice. The mixture was then subjected to Superose6 10/300 column (GE Healthcare). Fractions containing the quaternary complex ($RBD_{MACSp25}$/$RBD_{MACSp36}$-Fab_{B8}-Fab_{D14}-mACE2) were concentrated to 2mg/ml. The preparation method of the RBD_{MACSp6}/$RBD_{MACSp25}$/$RBD_{MACSp36}$-Fab_{B8}-Fab_{D14}-hACE2 complex is the same as that of the $RBD_{MACSp25}$/$RBD_{MACSp36}$-Fab_{B8}-Fab_{D14}-mACE2 complex.

Production of Fab fragment. The B8 and D14 Fab fragments [56] were generated using a Pierce FAB preparation Kit (Thermo Scientific). Briefly, the antibody was mixed with immobilized-papain and then digested at 37 ˚C for 3-4 h. The Fab was separated from the Fc fragment and undigested IgGs by protein A affinity column and then concentrated for analysis.

Surface plasmon resonance. mACE2 or hACE2 was immobilized onto a CM5 sensor chip surface using the NHS/EDC method to a level of ~600 response units (RUs) using BIAcore® 3000 (GE Healthcare) and PBS as running buffer (supplemented with 0.05% Tween-20). wtRBD, RBD_{MACSp6}, $RBD_{MACSp25}$ and $RBD_{MACSp36}$, which were purified and diluted, were injected in concentration from high to low. The binding responses were measured, they were regenerated with 10 mM Glycine, pH 1.5 (GE Healthcare). The apparent binding affinity (K_D) for individual antibody was calculated using BIAcore® 3000 Evaluation Software (GE Healthcare).

For the competitive binding assays, the first sample flew over the chip at a rate of 20 ul/min for 120 s, then the second sample was injected at the same rate for another 120s. All antibodies were evaluated at saturation concentration of 500 nM, mACE2 was at 1000 nM. All proteins were regenerated with 10 mM Glycine, pH 1.5 (GE Healthcare). The response units were recorded at room temperature and analyzed using the same software as mentioned above.

Cryo-EM sample preparation and data collection. For Cryo-EM sample preparation, the quaternary complex ($RBD_{MACSp25}/RBD_{MACSp36}$-$Fab_{B8}$-$Fab_{D14}$-mACE2 and $RBD_{MACSp6}/RBD_{MACSp25}/RBD_{MACSp36}$-$Fab_{B8}$-$Fab_{D14}$-hACE2 complex) was diluted to 0.8 mg/ml. Holy-carbon gold grid (Quantifoil R0.6/1.0 mesh 300) were freshly glow-discharged with a Solarus 950 plasma cleaner (Gatan) for 60s. A 3 μL aliquot of the mixture complex was transferred onto the grids, blotted with filter paper at 22□ and 100% humidity, and plunged into the ethane using a Vitrobot Mark IV (FEI). For these complex, micrographs were collected at 300 kV using a Titan Krios microscope (Thermo Fisher), equipped with a K2 detector (Gatan, Pleasanton, CA), using SerialEM automated data collection software [56]. Movies (32 frames, each 0.2 s, total dose 60 $e^-Å^{-2}$) were recorded at final pixel size of 1.04 Å with a defocus of between -1.25 and -2.7 μm.

Image processing. For $RBD_{MACSp25}$-Fab_{B8}-Fab_{D14}-mACE2 complex, a total of 2,109 micrographs were recorded. For $RBD_{MACSp36}$-Fab_{B8}-Fab_{D14}-mACE2 complex, a total of 2,982 micrographs were recorded. For $RBD_{MACSp6}/RBD_{MACSp25}/RBD_{MACSp36}$-$Fab_{B8}$-$Fab_{D14}$-hACE2 complex, the total of 2,005, 2,341 and 2659 micrographs were recorded, respectively. Both sets of the data were processed in the same way. Firstly, the raw data were processed by MotionCor2, which were aligned and averaged into motion-corrected summed images. Then, the defocus value for each micrograph was determined using Gctf. Next particles were picked and extracted for two-dimensional alignment. The partial well-defined particles were selected for initial model reconstruction in Relion. The initial model was used as a reference for three-dimensional classification. After the refinement and postprocessing, the overall resolution of $RBD_{MACSp36}$-Fab_{B8}-Fab_{D14}-mACE2 complex

was up to 3.69Å, on the basis of the gold-standard Fourier shell correlation (threshold = 0.143)[57]. For RBD$_{MACSp25}$-Fab$_{B8}$-Fab$_{D14}$-mACE2 complex, the ClassI complex was to 7.89 Å, ClassII complex was to 8.17 Å, ClassIII complex was to 4.4 Å. The final resolution of RBD$_{MACSp6}$-Fab$_{B8}$-Fab$_{D14}$-hACE2, RBD$_{MACSp25}$-Fab$_{B8}$-Fab$_{D14}$-hACE2 and RBD$_{MACSp36}$-Fab$_{B8}$-Fab$_{D14}$-hACE2 complex was up to 3.71 Å, 3.76 Å and 3.12 Å, respectively. The quality of the local resolution was evaluated by ResMap [58].

Model building and refinement. The RBD$_{WT}$-hACE2 (PDB ID: 6M0J) structures was manually docked into the refined maps of RBD$_{MACSp36}$-Fab$_{B8}$-Fab$_{D14}$-mACE2, RBD$_{MACSp6}$-Fab$_{B8}$-Fab$_{D14}$-hACE2, RBD$_{MACSp25}$-Fab$_{B8}$-Fab$_{D14}$-hACE2 and RBD$_{MACSp36}$-Fab$_{B8}$-Fab$_{D14}$-hACE2 complex using UCSF Chimera [59] and further corrected manually by real-space refinement in COOT [60]. The atomic models were further refined by positional and B-factor refinement in real space using Phenix [61]. Validation of the final model was performed with Molprobity [59]. The data sets and refinement statistics are shown in Supplementary table1 and Supplementary table3.

Infectivity assay of MASCp36 in HAE model. The resected cells were isolated from the airway specimens of patients and plated at a density of 250,000 cells per well on permeable Transwell-Col (12-mm-diameter) supports as previously described [62]. HAE cultures were generated in an air-liquid interface for 4-6 weeks to form well-differentiated, polarized cultures that resemble *in vivo* pseudostratified mucociliary epithelium. Prior to inoculation, the apical surface of well-differentiated HAE cells were washed three times with phosphate-buffered saline (PBS). The apical surface of cell cultures were inoculated with MASCp36 and its paretnal isolate WT (BetaCoV/Beijing/IMEBJ05/2020, Nos. GWHACBB01000000) at an MOI of 0.1 at 37℃ for 2 hours, and washed three times with PBS to remove the unbounded virus. HAE cells were cultured at an air-liquid interface at 37℃ with 5% CO_2. At 24, 48 and 72 hours post inoculation, 300 uL of PBS were applied to the apical surface of cell cultures and collected after an incubation for 10 minutes at 37℃. Viral RNA copies were quantified by real-time qPCR and shown as mean ± SD. WT or MASCp36 infected cells as well as uninfected cells were fixed with 4% paraformaldehyde,

permeabilized with Triton X100, and blocked with 10% BSA. The cells were then incubated with anti-SARS-CoV-2 N protein antibody (Sinobiological, 40143-R004, 1:1000) and HRP-conjugated secondary antibody, followed by DAPI staining. The percentage of SARS-CoV-2 N protein positive cells were shown as mean ± SD (n = 4).

Statistical analysis. Statistical analyses were carried out using Prism software (GraphPad). All data are presented as means ± standard error of the means (SEM). Statistical significance among different groups was calculated using the Student's t test, Fisher's Exact test, Two-way ANOVA or Mann-Whitney test *, **, and *** indicate $P < 0.05$, $P < 0.01$, and $P < 0.001$, respectively.

Data availability

The model has been deposited in the Protein Data Bank with accession code 7BBH [https://doi.org/10.2210/pdb7BBH/pdb]. All RNA-Seq data performed in this paper can be found on the NCBI Gene Expression Omnibus (GEO) under accession number GSE166778.

All the high throughput sequencing data and genome sequences related have been deposited in the National Genomics Data Center (https://bigd.big.ac.cn), BIG, CAS, with the BioSample accession number of SAMC341911-SAMC341915.

References:

1.   Moriarty LF, *et al.* Public Health Responses to COVID-19 Outbreaks on Cruise Ships - Worldwide, February-March 2020. *MMWR Morbidity and mortality weekly report* **69**, 347-352 (2020).

2.   Edler C, *et al.* Dying with SARS-CoV-2 infection-an autopsy study of the first consecutive 80 cases in Hamburg, Germany. *International journal of legal medicine* **134**, 1275-1284 (2020).

3.   Hanley B, Lucas SB, Youd E, Swift B, Osborn M. Autopsy in suspected COVID-19 cases. *Journal of clinical pathology* **73**, 239-242 (2020).

4.   Zhou B, *et al.* The pathological autopsy of coronavirus disease 2019 (COVID-2019) in China: a review. *Pathogens and disease* **78**,   (2020).

5.   Scully EP, Haverfield J, Ursin RL, Tannenbaum C, Klein SL. Considering how biological sex impacts immune responses and COVID-19 outcomes. *Nature reviews Immunology* **20**, 442-447 (2020).

6.   Liu K, Chen Y, Lin R, Han K. Clinical features of COVID-19 in elderly patients: A comparison with young and middle-aged patients. *The Journal of infection* **80**, e14-e18 (2020).

7.   Lan J, *et al.* Structure of the SARS-CoV-2 spike receptor-binding domain bound to the ACE2 receptor. *Nature* **581**, 215-220 (2020).

8.   Hu B, Guo H, Zhou P, Shi ZL. Characteristics of SARS-CoV-2 and COVID-19. *Nature reviews Microbiology*,   (2020).

9.   Ren W, *et al.* Comparative analysis reveals the species-specific genetic determinants of ACE2 required for SARS-CoV-2 entry. *PLoS pathogens* **17**, e1009392 (2021).

10.   Bao L, *et al.* The pathogenicity of SARS-CoV-2 in hACE2 transgenic mice. *Nature* **583**, 830-833 (2020).

11.   Israelow B, *et al.* Mouse model of SARS-CoV-2 reveals inflammatory role of type I interferon signaling. *The Journal of experimental medicine* **217**,   (2020).

12.   Sun J, *et al.* Generation of a Broadly Useful Model for COVID-19 Pathogenesis, Vaccination, and Treatment. *Cell* **182**, 734-743 e735 (2020).

13.   Gu H, *et al.* Adaptation of SARS-CoV-2 in BALB/c mice for testing vaccine efficacy. *Science* **369**, 1603-1607 (2020).

14.   Dinnon KH, 3rd, *et al.* A mouse-adapted model of SARS-CoV-2 to test COVID-19 countermeasures. *Nature* **586**, 560-566 (2020).

15.   Leist SR, *et al.* A Mouse-Adapted SARS-CoV-2 Induces Acute Lung Injury and Mortality in Standard Laboratory Mice. *Cell* **183**, 1070-1085 e1012 (2020).

16. Matute-Bello G, *et al.* An official American Thoracic Society workshop report: features and measurements of experimental acute lung injury in animals. *American journal of respiratory cell and molecular biology* **44**, 725-738 (2011).

17. Canete PF, Vinuesa CG. COVID-19 Makes B Cells Forget, but T Cells Remember. *Cell* **183**, 13-15 (2020).

18. Feng Z, *et al.* The Novel Severe Acute Respiratory Syndrome Coronavirus 2 (SARS-CoV-2) Directly Decimates Human Spleens and Lymph Nodes. *medRxiv*, 2020.2003.2027.20045427 (2020).

19. Diao B, *et al.* Human Kidney is a Target for Novel Severe Acute Respiratory Syndrome Coronavirus 2 (SARS-CoV-2) Infection. *medRxiv*, 2020.2003.2004.20031120 (2020).

20. Klein SL. Immune cells have sex and so should journal articles. *Endocrinology* **153**, 2544-2550 (2012).

21. Lv Z, *et al.* Structural basis for neutralization of SARS-CoV-2 and SARS-CoV by a potent therapeutic antibody. *Science* **369**, 1505-1509 (2020).

22. Wang J, *et al.* Mouse-adapted SARS-CoV-2 replicates efficiently in the upper and lower respiratory tract of BALB/c and C57BL/6J mice. *Protein & cell* **11**, 776-782 (2020).

23. Bradley BT, *et al.* Histopathology and ultrastructural findings of fatal COVID-19 infections in Washington State: a case series. *Lancet* **396**, 320-332 (2020).

24.   Kumar A, *et al.* Clinical Features of COVID-19 and Factors Associated with Severe

Clinical Course: A Systematic Review and Meta-Analysis. *Ssrn*, 3566166 (2020).

25.   Tian S, *et al.* Pathological study of the 2019 novel coronavirus disease (COVID-19)

through postmortem core biopsies. *Modern pathology : an official journal of the United

States and Canadian Academy of Pathology, Inc* **33**, 1007-1014 (2020).

26.   Xu Z, *et al.* Pathological findings of COVID-19 associated with acute respiratory

distress syndrome. *The Lancet Respiratory medicine* **8**, 420-422 (2020).

27.   Pan XW, Xu D, Zhang H, Zhou W, Wang LH, Cui XG. Identification of a potential

mechanism of acute kidney injury during the COVID-19 outbreak: a study based on

single-cell transcriptome analysis. *Intensive care medicine* **46**, 1114-1116 (2020).

28.   Perico L, Benigni A, Casiraghi F, Ng LFP, Renia L, Remuzzi G. Immunity, endothelial

injury   and   complement-induced   coagulopathy   in   COVID-19.   *Nature   reviews

Nephrology* **17**, 46-64 (2021).

29.   Ellul MA, *et al.* Neurological associations of COVID-19. *The Lancet Neurology* **19**,

767-783 (2020).

30.   Nicholls JM, *et al.* Lung pathology of fatal severe acute respiratory syndrome. *Lancet*

361, 1773-1778 (2003).

31.   Wu F, *et al.* A new coronavirus associated with human respiratory disease in China.

Nature **579**, 265-269 (2020).

32.   Fineberg HV. Pandemic preparedness and response--lessons from the H1N1

        influenza of 2009. *The New England journal of medicine* **370**, 1335-1342 (2014).

33.   World Health Organization W. Report of the WHO-China Joint Mission on Coronavirus

        Disease 2019 (COVID-19).) (2020).

34.   Chen Y, Li L. SARS-CoV-2: virus dynamics and host response. *The Lancet Infectious

        diseases* **20**, 515-516 (2020).

35.   Furman D, *et al.* Chronic inflammation in the etiology of disease across the life span.

        Nature medicine **25**, 1822-1832 (2019).

36.   Tan M, *et al.* Immunopathological characteristics of coronavirus disease 2019 cases in

        Guangzhou, China. *Immunology* **160**, 261-268 (2020).

37.   Kamiya Y, *et al.* Influenza A virus enhances ciliary activity and mucociliary clearance

        via TLR3 in airway epithelium. *Respiratory research* **21**, 282 (2020).

38.   Bustamante-Marin XM, Ostrowski LE. Cilia and Mucociliary Clearance. *Cold Spring

        Harbor perspectives in biology* **9**,   (2017).

39.   Whitsett JA. Airway Epithelial Differentiation and Mucociliary Clearance. *Annals of the

        American Thoracic Society* **15**, S143-S148 (2018).

40.   Lee IT, *et al.* ACE2 localizes to the respiratory cilia and is not increased by ACE

        inhibitors or ARBs. *Nature communications* **11**, 5453 (2020).

41.   Dudley JP, Lee NT. Disparities in Age-specific Morbidity and Mortality From SARS-CoV-2 in China and the Republic of Korea. *Clinical infectious diseases : an official publication of the Infectious Diseases Society of America* **71**, 863-865 (2020).

42.   Epicentro L'epidemiologia per la sanità pubblica Istituto Superiore di Sanità. Characteristics of COVID-19 patients dying in Italy Report based on available data on March 20th.) (2020).

43.   Marquez EJ, Trowbridge J, Kuchel GA, Banchereau J, Ucar D. The lethal sex gap: COVID-19. *Immunity & ageing : I & A* **17**, 13 (2020).

44.   Channappanavar R, Fett C, Mack M, Ten Eyck PP, Meyerholz DK, Perlman S. Sex-Based Differences in Susceptibility to Severe Acute Respiratory Syndrome Coronavirus Infection. *Journal of immunology* **198**, 4046-4053 (2017).

45.   Klein SL, Flanagan KL. Sex differences in immune responses. *Nature reviews Immunology* **16**, 626-638 (2016).

46.   Rahman MS, *et al.* Evolutionary dynamics of SARS-CoV-2 nucleocapsid protein (N protein) and its consequences. *bioRxiv*, 2020.2008.2005.237339 (2020).

47.   Criado PR, Pagliari C, Carneiro FRO, Quaresma JAS. Lessons from dermatology about inflammatory responses in Covid-19. *Reviews in medical virology* **30**, e2130 (2020).

48.   Bhat EA, *et al.* SARS-CoV-2: Insight in genome structure, pathogenesis and viral

        receptor binding analysis - An updated review. *International immunopharmacology* **95**,

        107493 (2021).

49.   Chen Y, Liu Q, Guo D. Emerging coronaviruses: Genome structure, replication, and

        pathogenesis. *Journal of medical virology* **92**, 418-423 (2020).

50.   Xia H, *et al.* Evasion of Type I Interferon by SARS-CoV-2. *Cell reports* **33**, 108234

        (2020).

51.   Plante JA, *et al.* Spike mutation D614G alters SARS-CoV-2 fitness. *Nature*,   (2020).

52.   Davies NG, *et al.* Estimated transmissibility and impact of SARS-CoV-2 lineage

        B.1.1.7 in England. *Science* **372**,   (2021).

53.   Tegally H, *et al.* Emergence and rapid spread of a new severe acute respiratory

        syndrome-related coronavirus 2 (SARS-CoV-2) lineage with multiple spike mutations

        in South Africa. *medRxiv*, 2020.2012.2021.20248640 (2020).

54.   Castonguay N, Zhang W, Langlois M-A. Meta-Analysis of the Dynamics of the

        Emergence   of   Mutations   and   Variants   of   SARS-CoV-2.   *medRxiv*,

        2021.2003.2006.21252994 (2021).

55.   Wolfel R, *et al.* Virological assessment of hospitalized patients with COVID-2019.

        Nature **581**, 465-469 (2020).

56.   Pettersen EF, *et al.* UCSF Chimera--a visualization system for exploratory research

        and analysis. *Journal of computational chemistry* **25**, 1605-1612 (2004).

57.   Brown A, Long F, Nicholls RA, Toots J, Emsley P, Murshudov G. Tools for macromolecular model building and refinement into electron cryo-microscopy reconstructions. *Acta crystallographica Section D, Biological crystallography* **71**, 136-153 (2015).

58.   Afonine PV, *et al.* Towards automated crystallographic structure refinement with phenix.refine. *Acta crystallographica Section D, Biological crystallography* **68**, 352-367 (2012).

59.   Chen VB, *et al.* MolProbity: all-atom structure validation for macromolecular crystallography. *Acta crystallographica Section D, Biological crystallography* **66**, 12-21 (2010).

60.   Scheres SH. RELION: implementation of a Bayesian approach to cryo-EM structure determination. *Journal of structural biology* **180**, 519-530 (2012).

61.   Mastronarde DN. Automated electron microscope tomography using robust prediction of specimen movements. *Journal of structural biology* **152**, 36-51 (2005).

62.   Zhu N, *et al.* Morphogenesis and cytopathic effect of SARS-CoV-2 infection in human airway epithelial cells. *Nature communications* **11**, 3910 (2020).

63.   Kucukelbir A, Sigworth FJ, Tagare HD. Quantifying the local resolution of cryo-EM density maps. *Nature methods* **11**, 63-65 (2014).

Acknowledgements

Author contributions

S.S., H.G., L.C., Q.C., Q.Y.,G.Y., R.-T.L., H.F., Y.-Q.D., X.S., Y.Q., M.L., J.L., R.F., Y.G., N.Z., S.Q., L.W., Y.-F.Z., C.Z., L.Z., Y.C., and M.S. performed experiments; S.S., H.G., Q.C., G.Y., R.-T.L., H.F, Y.C., X.Y., X.W., W.T., and H.W. analyzed data. C.-F.Q., X.W., H.G., and S.S conceived the project and designed the experiments. S.S. and H.G., and R.-T.L. wrote the draft of the manuscript. C.-F.Q., and X.W. supervised the study and wrote the manuscript with the input of all co-authors.

Competing interests

All authors have no competing interests

Data and materials availability

All requests for resources and reagents should be directed to C.-F.Q. (qincf@bmi.ac.cn or qinlab313@163.com) and will be fulfilled after completion of a materials transfer agreement.

Figure 1
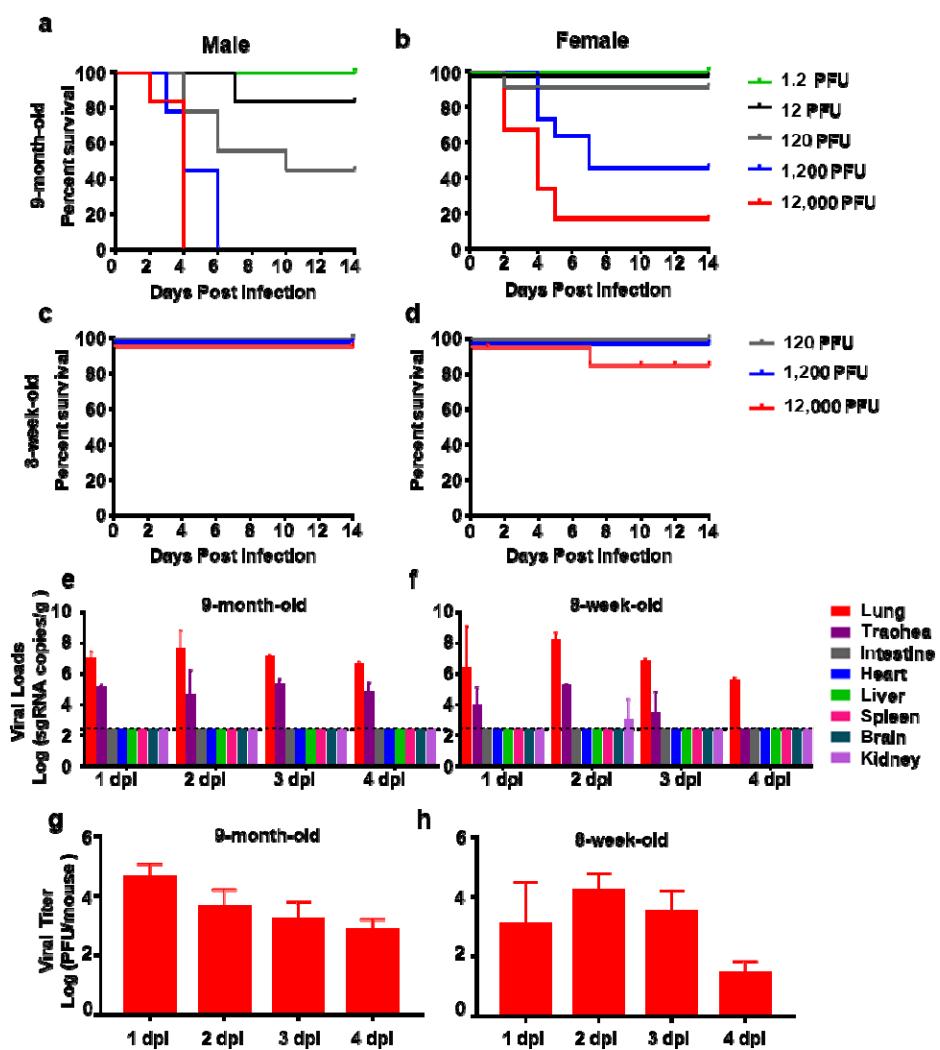
Fig 1. MASCp36 is highly virulent in 9-month-old mice. a-d Survival curve of BALB/c mice upon challenge with MASCp36. Groups of female or male 9-month-old BALB/c mice and 8-week-old BALB/c mice were infected intranasally with the indicated doses of MASCp36, and the clinical symptoms and mortality were recorded for 14 days (n≥6 per group). **e-f** Replication dynamics and tissue distribution of SARS-CoV-2 sgRNAs in mice infected with MASCp36. Groups of 9-month-old BALB/c mice were *i.n.* inoculated with 12,000 PFU of MASCp36, and sacrificed at 4 dpi. All the indicated tissue samples were collected and subjected to viral sgRNA load analysis by qRT-PCR. Dash lines denote the detection limit. Data are presented as

means ± SEM (n=4 per group). **g-h** Infectious viral titers in lung tissues in mice infected with MASCp36 were detected by plaque formation assay. Data are presented as means ± SEM (n=4 per group).

Figure 2
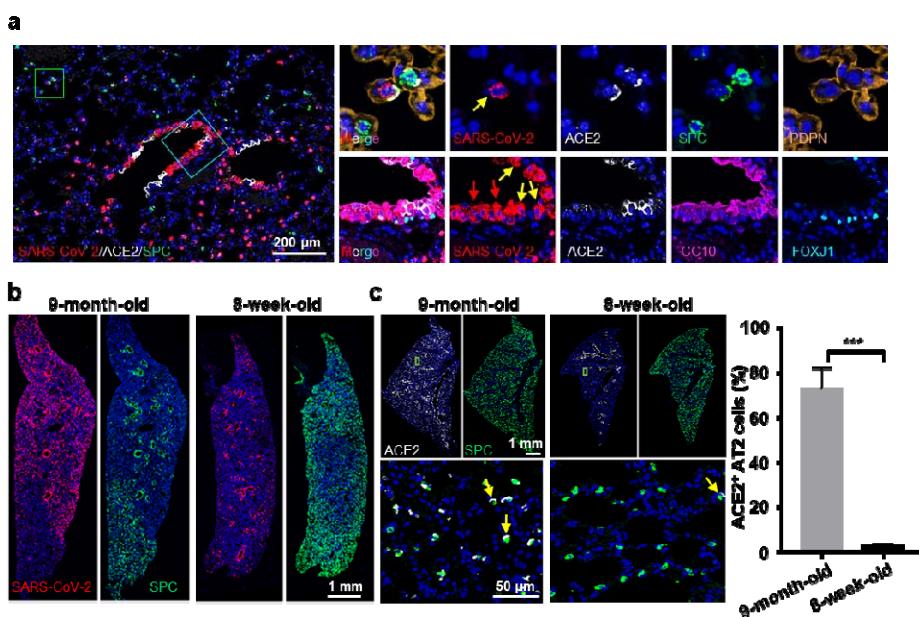
Fig 2. Difference of MASCp36 cellular tropism in lungs from 9-month-old and 8-week-old mice. a Multiplex immunofluorescence staining for detection of SARS-CoV-2 targeted cells in lung sections of male mouse (9-month-old) at 1 dpi. SARS-CoV-2 N protein (red), ACE2 (white), SPC (green), PDPN (gold), CC10 (magenta), FOXJ1 (cyan). The framed areas are shown adjacently at a higher magnification. The yellow arrows indicate ACE2$^+$ club cells infected with SARS-CoV-2, and the red arrows indicate decreased ACE2 expression in infected cells. **b** Multiplex immunofluorescence staining of lung sections for SARS-CoV-2 N protein (red) and SPC (green) detection in male mice at 1 dpi. **c** Multiplex immunofluorescence staining for detection of ACE2 (white) and SPC (green) expression in lung tissues from the un-infected control mice (9-month-old and 8-week-old). The framed areas are shown below at a higher magnification. The yellow arrows indicate ACE2$^+$ cells. The percentage of ACE2$^+$ cells in the SPC$^+$ AT2 compartment was statistically analyzed. Data are presented as mean $\pm$ SD (n = 3 per group).

Figure 3
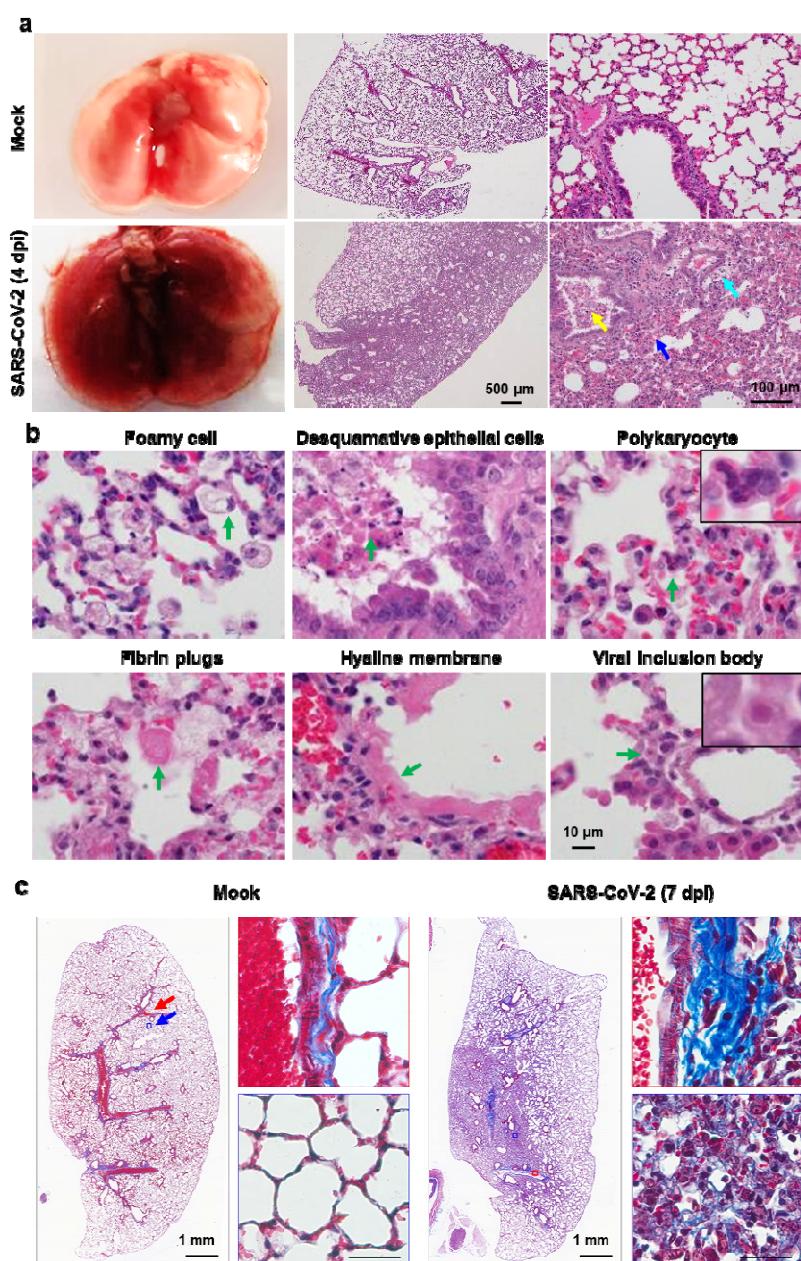
Fig 3. Acute lung damage caused by MASCp36 infection in mice. a Gross necropsy and hematoxylin and eosin (H&E) staining of lung sections from male BALB/c mice (9-month-old) infected with 1,200 PFU of MASCp36. Yellow arrow indicates desquamative epithelial cells in bronchiole tubes, cyan arrow indicates edema around vessels and blue arrow indicates hemorrhage. Representative images are shown ）.(n=3 per group). **b** Microscopic observation of lungs showing foamy cells,

desquamative epithelial cells, polykaryocytes, fibrin plugs, hyaline membrane and viral inclusion body. **c** Masson's trichrome staining of lung sections from male BALB/c mice (9-month-old) infected with 120 PFU of MASCp36 (n=5 per group) at 7 dpi. Framed areas are shown adjacently at higher magnification.

Figure 4
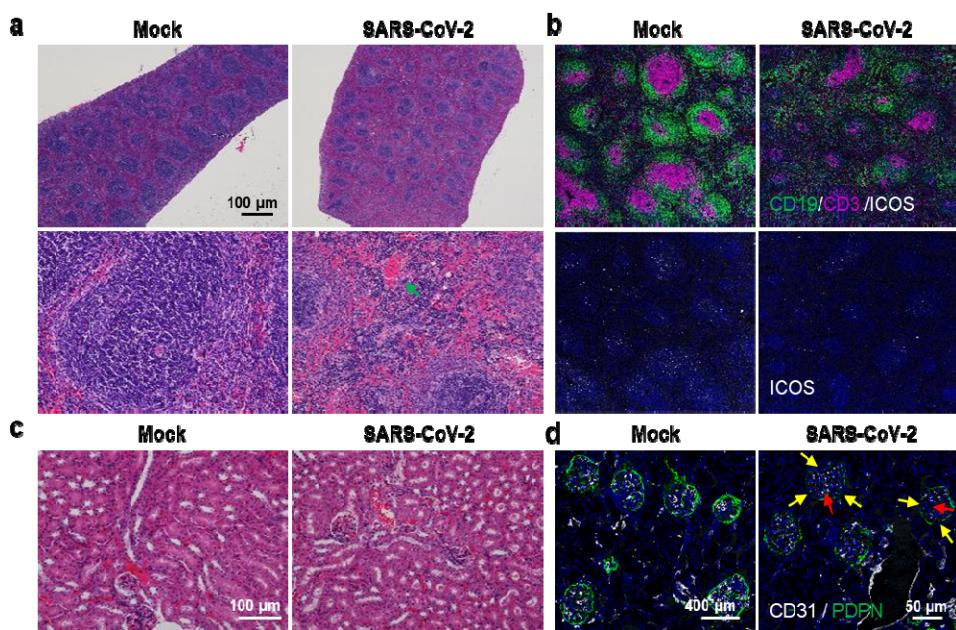
Fig 4. Spleen and kidney injury during BALB/c mice infection with MASCp36. a H&E staining of spleen sections from male BALB/c mice (9-month-old) infected with MASCp36. **b** Multiplex immunofluorescence staining of mouse spleen sections for detection of CD19 (green) B cells, CD3 (magenta) T cells and ICOS (white) follicular helper T cells. **c** H&E staining of kidney sections from male BALB/c mice (9-month-old) infected with MASCp36 at 4 dpi (n=3 per group). **d** Multiplex immunofluorescence staining of mouse kidney sections for CD31(white) and PDPN (green). The yellow and red arrows indicate discrete glomerular basement membrane and endothelial vessels, respectively.

Figure 5
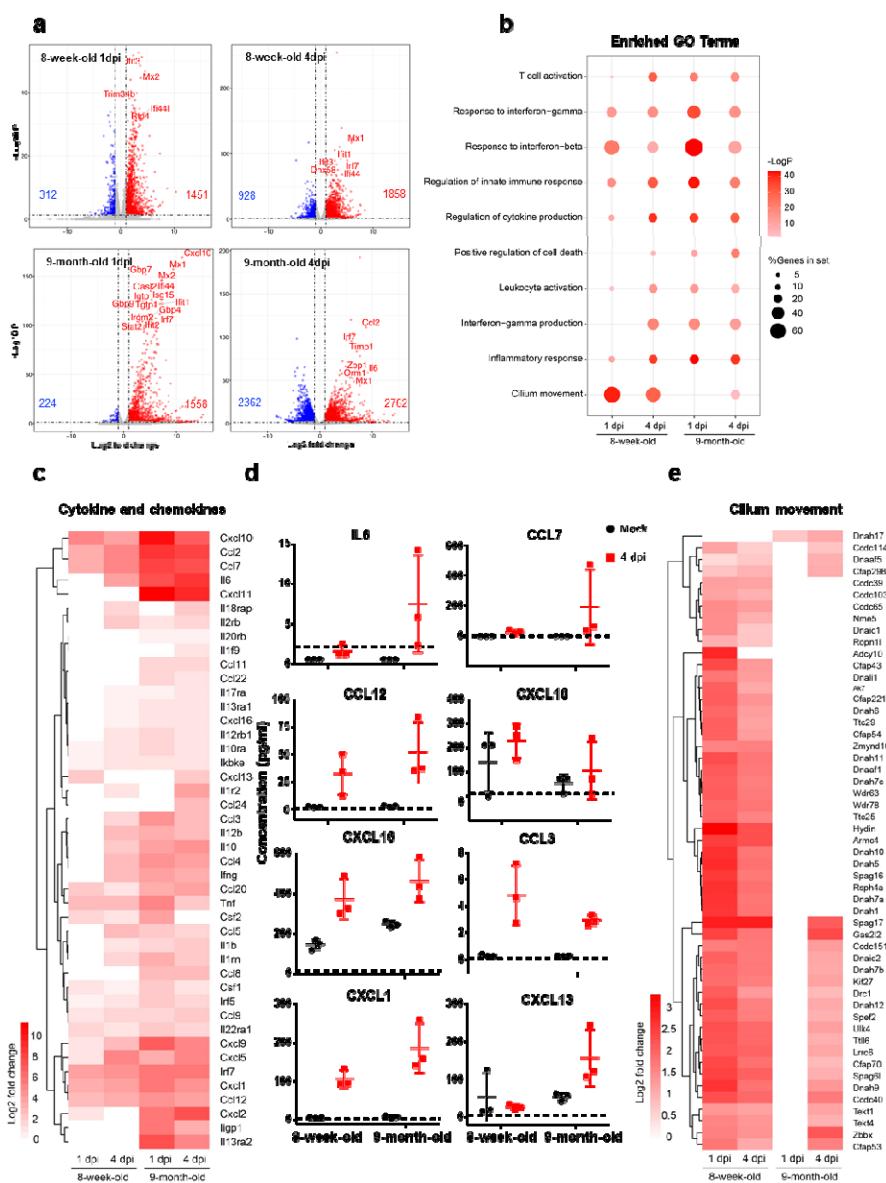
Fig 5. Host transcriptional response to MASCp36 in lungs of 8-week-old and 9-month-old male BALB/c mice. **a** Volcano plots indicating differential regulated genes after MASCp36 infection at 1 and 4 dpi. Up-regulated genes (padj < 0.05) with a log2 (fold change) of more than 1 are indicated in red, down-regulated genes (padj < 0.05) with a log2 (fold change) of less than -1 are indicated in blue. Among the top 20 up-regulated genes, interferon stimulated genes (ISGs) and cytokines were marked with gene symbols. **b** Dot plot visualization of enriched GO terms of up-regulated

genes at 1 and 4 dpi. Gene enrichment analyses were performed using Metascape against the GO dataset for biological processes. The color of the dots represents the -LogP value for each enriched GO term, and size represents the percentage of genes enriched in each GO term. **c** Heatmap indicating the expression patterns of genes belonging to GO annotation for cilium movement. **d** Male BALB/c mice (8-week-old and 9-month-old) were i.n. inoculated with 12,000 PFU of MASCp36, and lung homogenates were prepared at 4 dpi (n=3 per group). Cytokine and chemokine analysis was determined by Luminex. Dash lines denote the detection limit. **e** Heatmap indicating the expression patterns of 44 cytokine and chemokine genes. c and d depict the log2(fold change) of genes of infected compared with mock-infected mice. The log2(fold change) of not significantly changed genes (padj > 0.05) were counted as zero.

Figure 6
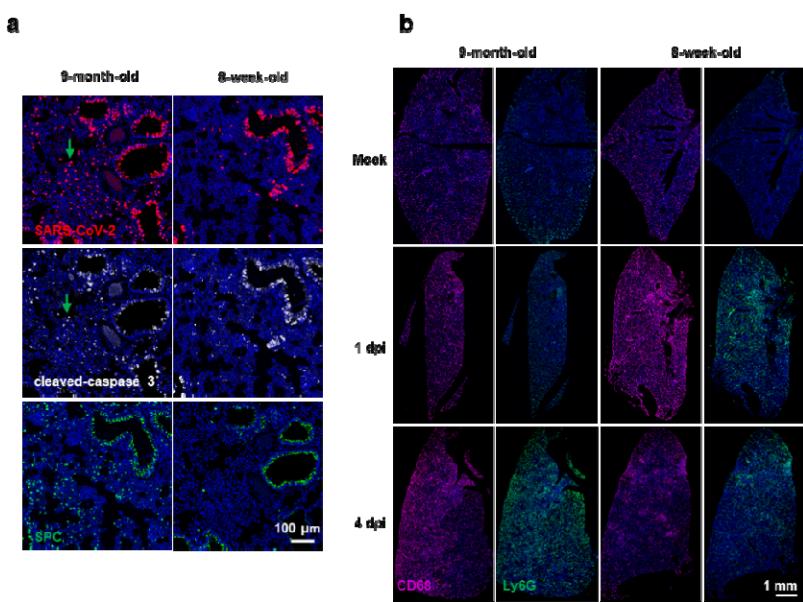
Fig 6. Lung specific response of 8-week-old and 9-month-old male BALB/c mice during MASCp36 infection. a Multiplex immunofluorescence staining for detection of SARS-CoV-2 N protein (red), cleaved-caspase 3 (white) and SPC (green) expression in lung tissues of male mice (9-month-old and 8-week-old) at 1 dpi. The green arrows indicate apoptotic cells with MASCp36 infection in the alveolar region (n=3 per group) **b** Multiplex immunofluorescence staining for CD68$^+$ macrophages and Ly-6G$^+$ neutrophils infiltration in 9-month-old mice and 8-week-old mice after infection at 1 dpi and 4 dpi. Less CD68$^+$ macrophages and Ly-6G$^+$ neutrophils were detected in 9-month-old mice than that in young mice 1 dpi, and reversed on 4 dpi (n=3 per group).

Figure 7
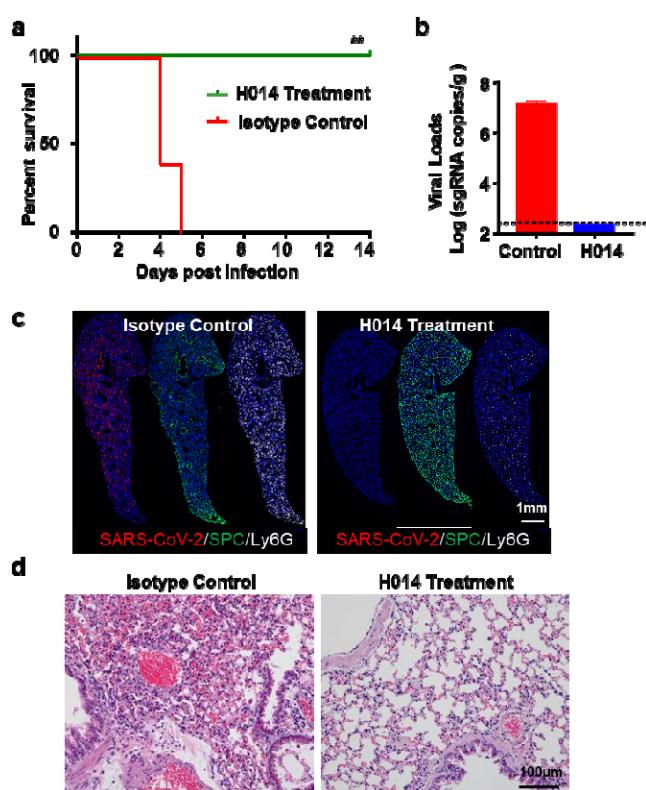
Fig 7. The efficacy of H014 against MASCp36 infection. Male BALB/c mice (9-month-old) infected with 1,200PFU of MASCp36. **a** survival curves of mice in H014 and mock treatment groups (n=5 per group). Statistical significance was analyzed by Student's t test. **b** Lung samples were collected at 4 dpi and subjected to viral RNA load analysis by RT-qPCR. Dash lines denote the detection limit. (n=3 per group) **c** Multiplex immunofluorescence staining of mouse lung sections for detection of SARS-CoV-2 N protein (red), SPC (green) and Ly6G (white) **d** H&E staining of lung sections from H014 or isotype control (n=3 per group).

Figure 8
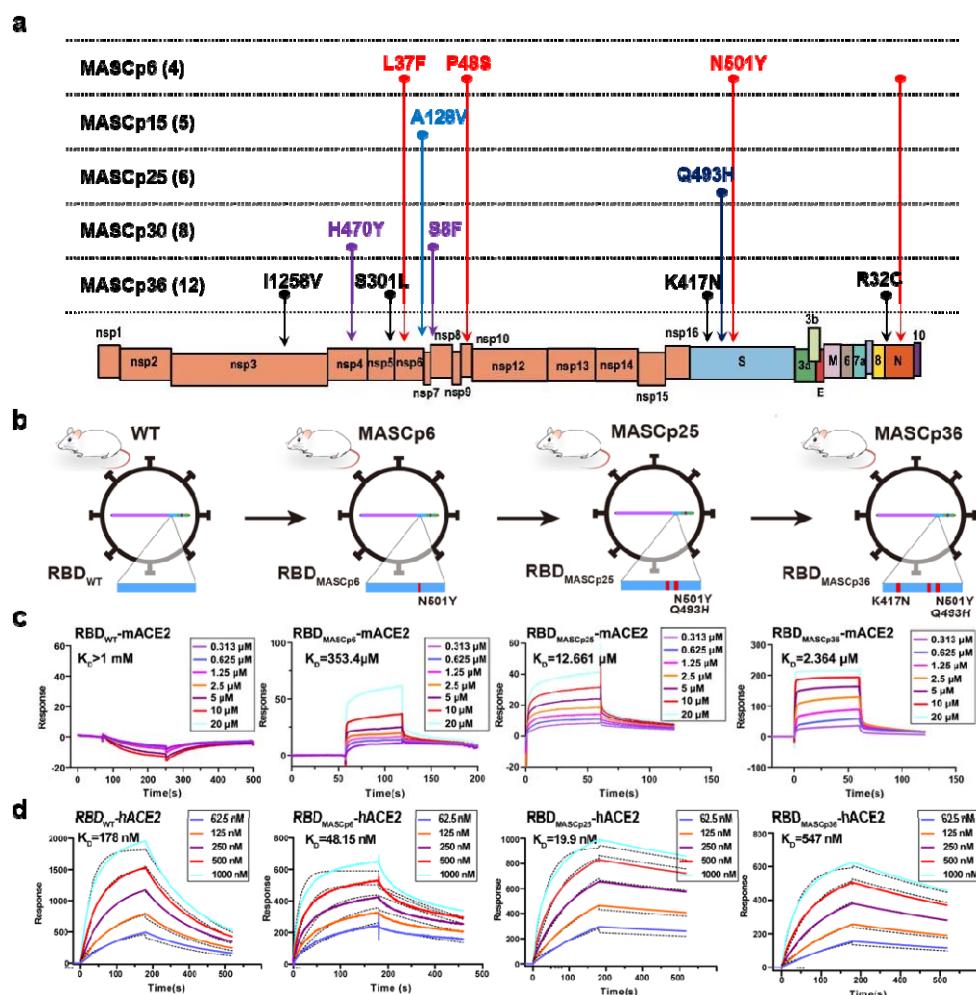
Fig 8. Adaptive RBD mutations identified in different mouse adapted strains. **a**. Schematic diagram of SARS-CoV-2 genome and all the adaptive mutations. **b** Schematic diagram depicting virus harboring different RBD mutations. The mutation site is marked with a red rectangle. b The proportion of N501Y, Q493H, K417N mutations located on the RBD. **c,d** Binding properties of RBDWT, RBDMASCp6, RBDMASCp25 and RBDMASCp36 to mACE2 and hACE2 analyzed using SPR. For both panels, mACE2 was loaded onto the sensor; RBDWT, RBDMASCp6, RBDMASCp25 and RBDMASCp36 were injected. Response units were plotted against protein concentrations. The KD values were calculated by BIAcore® 3000 analysis software (BIAevaluation version 4.1).

Figure 9
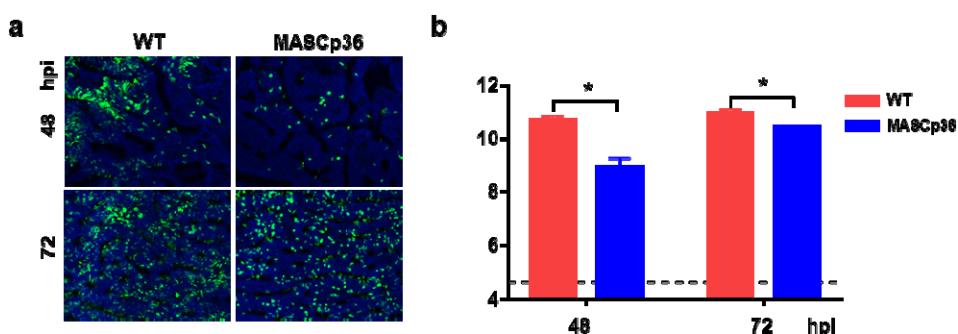
Fig.9 Characterization of MASCp6 and MASCp36 in human airway epithelial (HAE) cells. a Growth kinetics of WT (BetaCoV/Beijing/IMEBJ05/2020, Nos. GWHACBB01000000) and MASCp36 in HAE at 48 and 72h post infection. Results are shown as mean±SD from two independent replicates. **b** Immunofluorescence staining of WT and MASCp36 infected HAE cultures for SARS-CoV-2 N protein (green) and DAPI (blue) at 48 and 72h post infection. The percentage of SARS-CoV-2 N protein positive cells were presented as mean±SD (n = 4).

Figure 10
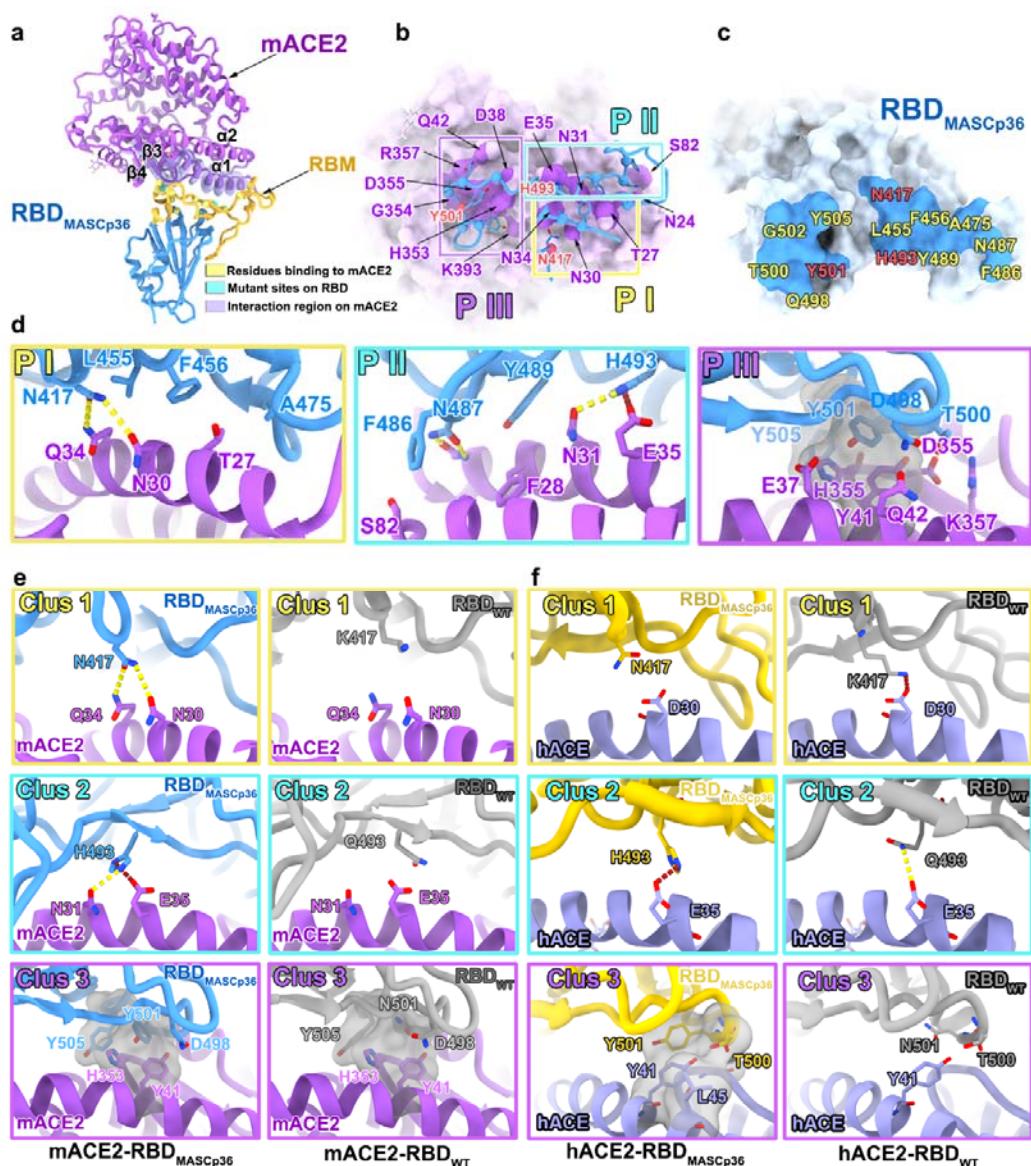
Fig.10 Mechanism of binding of SARS-CoV-2 derived MASCp36 to mACE2. a Overall structure of RBDMASCp36 bound to mACE2. Residues of RBDMASCp36 participating in the binding to mACE2 are shown as spheres and colored in yellow, the mutation sites are colored in cyan, the RBM is colored in gold. The region of mACE2 responsible for binding is labelled. **b and c** The binding interface between RBDMASCp36 and mACE2. The residues involved in binding to mACE2 are presented as sticks, and the residues of mACE2 interacting with RBDMASCp36 are

shown as surface. The mutated residues in RBDMASCp36 are colored in red. **d** Details of the interactions between RBDMASCp36 and mACE2. Some residues involved in the formation of hydrophobic patches (grey mesh), salt bridge (red dash) and hydrogen bonds (yellow dash) are shown as sticks and labeled. **e** The comparison of interactions at RBDWT-mACE2 and RBDMASCp36-mACE2 interface. RBDWT, RBDMASCp36 and mACE2 are colored in grey, cyan and purple, respectively. The residues involved in the formation of hydrophobic patches (grey mesh), salt bridge (red dash) and hydrogen bonds (yellow dash) are shown as sticks and labeled. **f.** The comparison of interactions at RBDWT-hACE2, RBDMASCp6- hACE2, RBDMASCp25-hACE2 and RBDMASCp36-hACE2 interface. RBDWT, RBDMASCp6, RBDMASCp25 and RBDMASCp36 are colored in grey, red, yellow, and cyan, respectively.

Supplementary Materials for

Characterization and structural basis of a lethal mouse-adapted SARS-CoV-2

Shihui Sun[1†], Hongjing Gu[1†], Lei Cao[2†], Qi Chen[1†], Qing Ye[1†], Guan Yang[3†], Rui-Ting Li[1†], Hang Fan[1†],Yong-Qiang Deng[1], Xiaopeng Song[3], Yini Qi[3], Min Li[1], Jun Lan[2], Rui Feng[2], Yan Guo[1], Na Zhu[4], Si Qin[1], Lei Wang[2], Yi-Fei Zhang[1], Chao Zhou[1], Lingna Zhao[1], Yuehong Chen[1], Meng Shen[1], Yujun Cui[1], Xiao Yang[3], Xinquan Wang[5], Wenjie Tan[4], Hui Wang[1*], Xiangxi Wang[2*], Cheng-Feng Qin[1,6*]

Correspondence to: Cheng-Feng Qin (qincf@bmi.ac.cn), Xiangxi Wang (xiangxi@ibp.ac.cn), or Hui Wang (geno0109@vip.sina.com)

**This PDF file includes:**

Supplementary Figure 1 to 11

Supplementary Table 1 to 3

Supplementary Figure 1
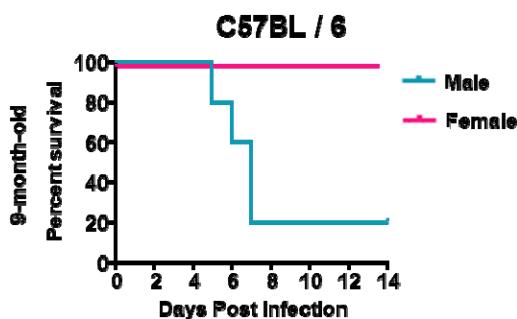
Supplementary Figure 1. Gender dependent mortality in MASCp36-infected C57BL/6 mice at age of 9 months. Survival curves of male and female C57BL/6 mice infected with 12,000 PFU of MASCp36 (n=5 per group).

.

Supplementary Figure 2
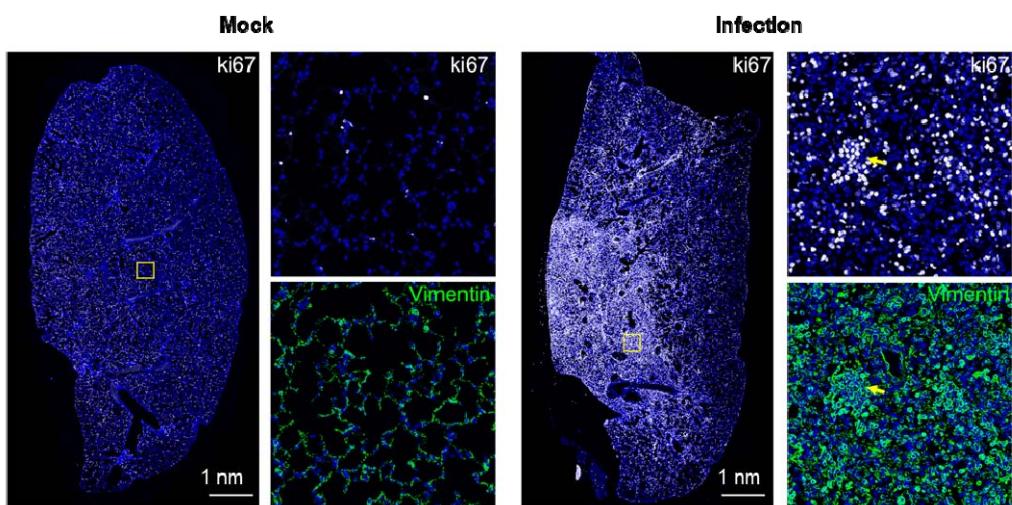
Supplementary Figure 2. MASCp36 infection causes proliferation of alveolar mesenchymal cells in lung of BALB/c mice. Multiplex immunofluorescence staining of lung sections from 9-month-old BALB/c mice infected with 120 PFU of MASCp36. The proliferation marker ki67 and mesenchymal marker Vimentin were shown in white and green, respectively. Framed areas are shown adjacently at higher magnifications. Arrows indicate proliferating alveolar mesenchymal cells (n=5 per group).

Supplementary Figure 3
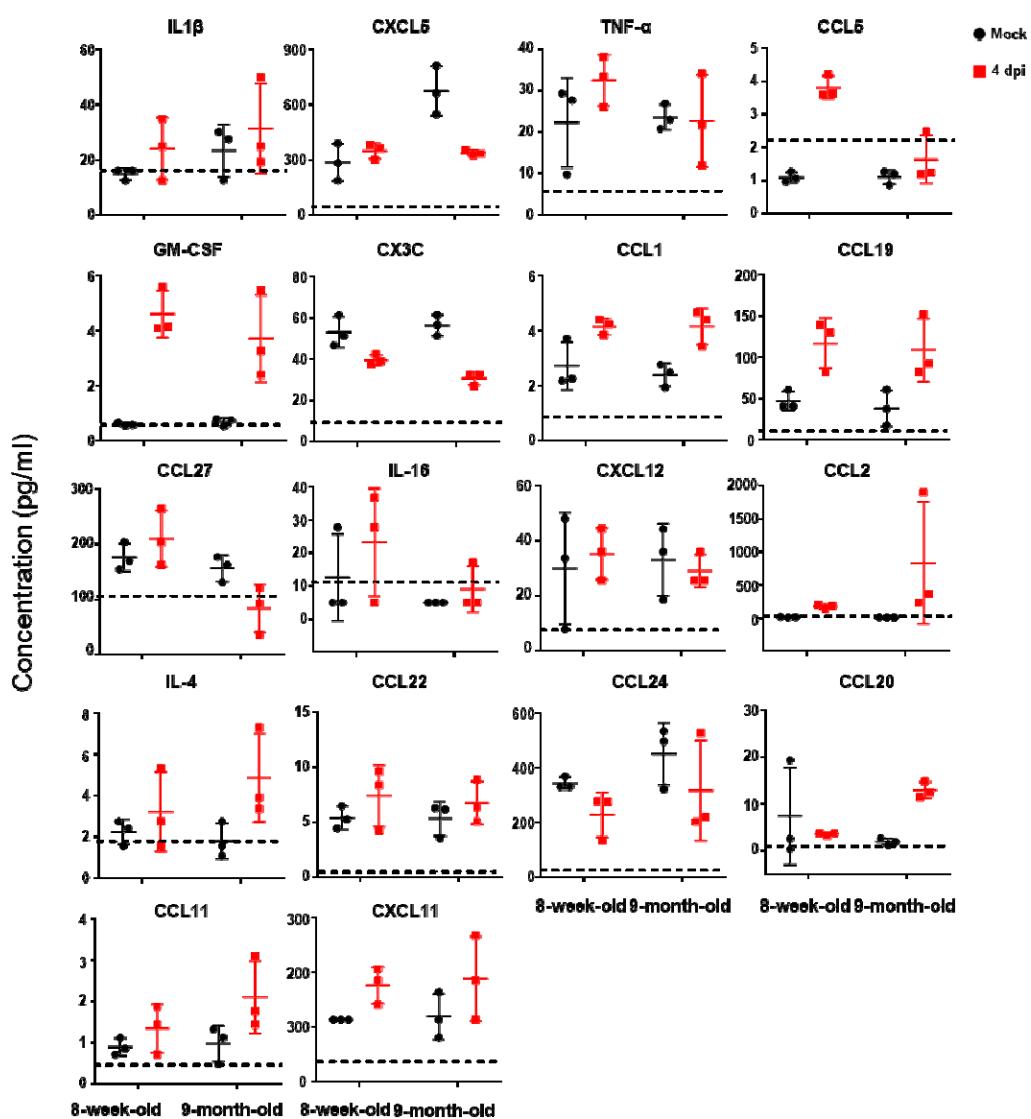
Supplementary Figure 3. Pulmonary cytokine and chemokine in mice infected with MASCp36. Male BALB/c mice (8-week-old and 9-month-old) were i.n. inoculated with 12,000 PFU of MASCp36, and lung homogenates were prepared at 4 dpi (n=3 per group). Cytokine and chemokine analysis was determined by Luminex. Dash lines denote the detection limit.

Supplementary Figure 4
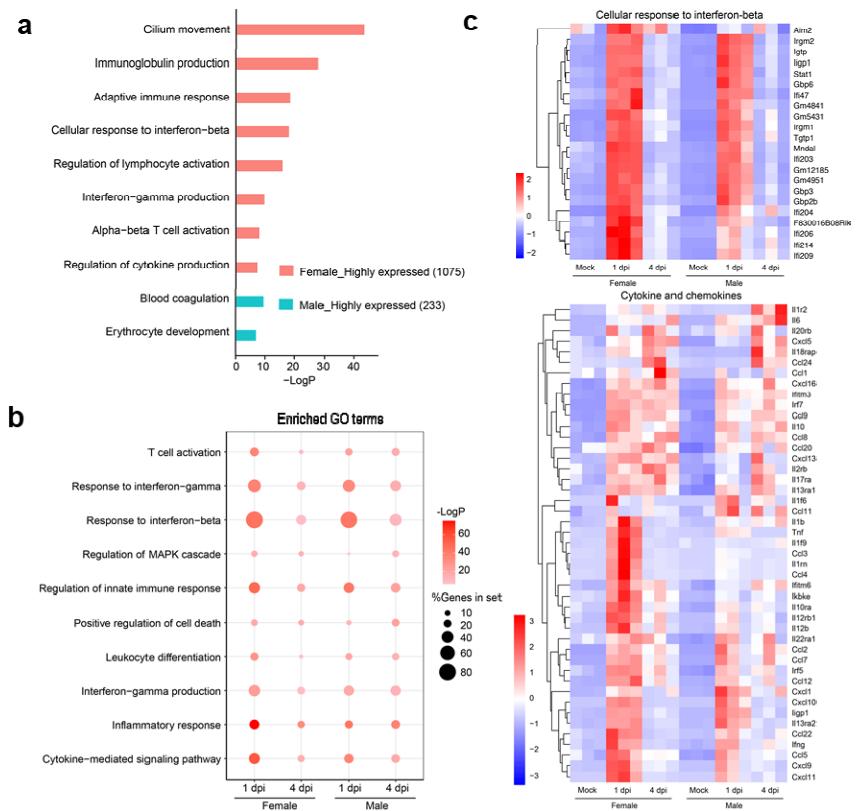
Supplementary Figure 4. Comparison of host transcriptional response to MASCp36 in lungs of female and male 9-month-old BALB/c mice. **a.** Enriched GO terms of DEGs when comparing non-infected male and female transcriptome. **b.** Dot plot visualization of enriched GO terms of up-regulated genes at 1 and 4 dpi. Gene enrichment analyses were performed using Metascape against the GO dataset for biological processes. The color of the dots represents the -LogP value for each enriched GO term, and size represents the percentage of genes enriched in each GO term. **c.** Heatmap indicating the expression patterns of genes belonging to GO annotation for "cellular response to interferon-beta" and 44 cytokine/chemokine genes. Colored bar represents Z-score of TPM

Supplementary Figure 5
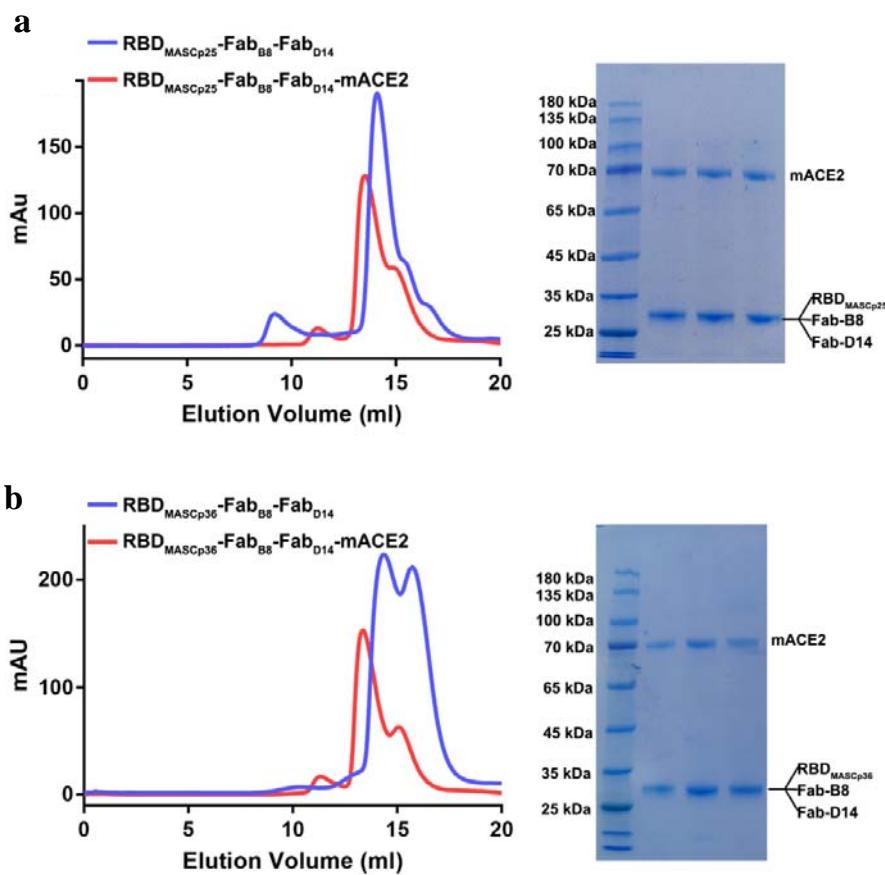
Supplementary Figure 5. Purification and characterization of RBD$_{MASCp25}$-Fab$_{B8}$-Fab$_{D14}$-mACE2 complex and RBD$_{MASCp36}$-Fab$_{B8}$-Fab$_{D14}$-mACE2 complex. a Gel filtration profiles of the ternary complex (RBD$_{MASCp25}$-Fab$_{B8}$-Fab$_{D14}$, colored by blue line) and quaternary complex (RBD$_{MASCp25}$-Fab$_{B8}$-Fab$_{D14}$-mACE2, colored by red line). SDS-PAGE analysis of the RBD$_{MASCp25}$-Fab$_{B8}$-Fab$_{D14}$-mACE2 complex. **b** Gel filtration profiles of the ternary complex (RBD$_{MASCp36}$-Fab$_{B8}$-Fab$_{D14}$, colored by bule line) and quaternary complex (RBD$_{MASCp36}$-Fab$_{B8}$-Fab$_{D14}$-mACE2, colored by red line). SDS-PAGE analysis of the RBD$_{MASCp36}$-Fab$_{B8}$-Fab$_{D14}$-mACE2 complex.

**Supplementary Figure 6**
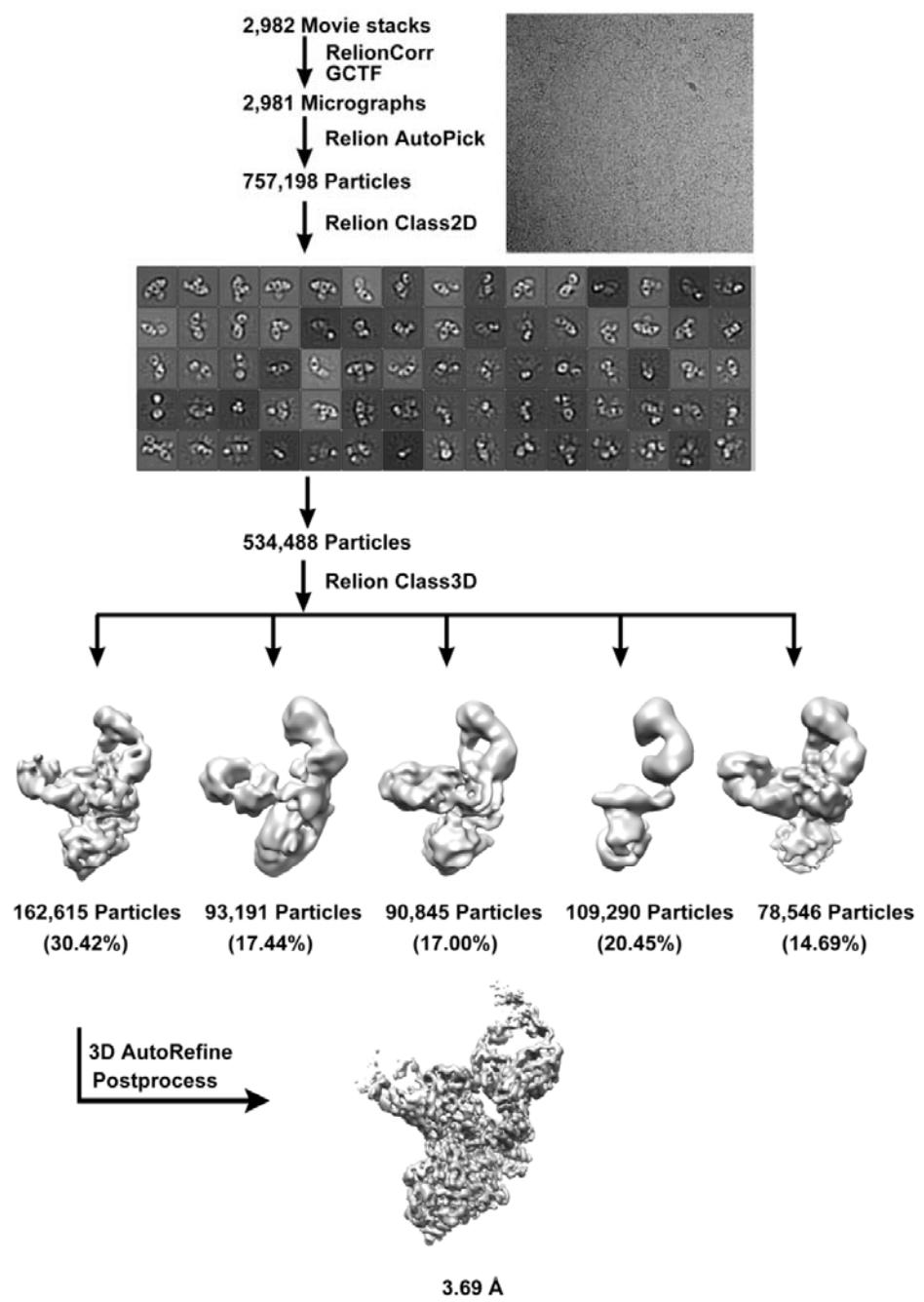
Supplementary Figure 6. Flow chart for the Cryo-EM data processing of RBD$_{MASCp36}$-Fab$_{B8}$-Fab$_{D14}$-mACE2 complex.

Supplementary Figure 7
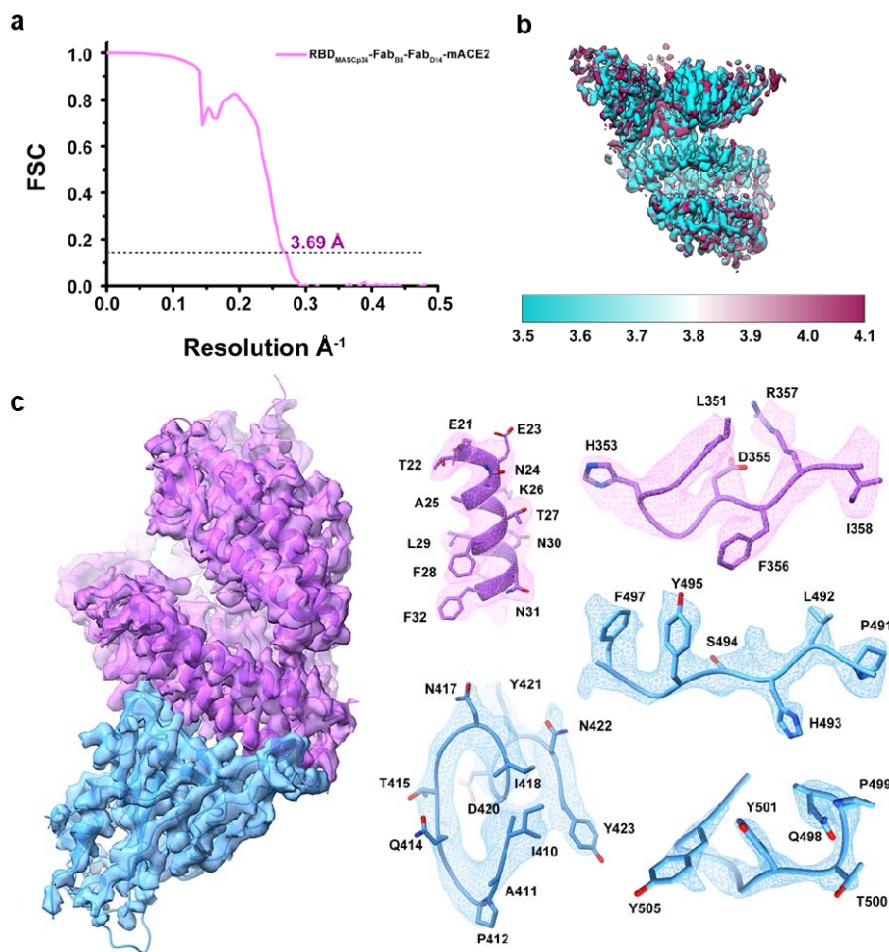
Supplementary Figure 7. Cryo-EM images and resolution evaluation of the EM map of RBD$_{MASCp36}$-Fab$_{B8}$-Fab$_{D14}$-mACE2 complex. a The gold-standard FSC curve of the final map. **b** Local resolution assessments of cryo-EM maps. Local-resolution evaluation of the map of the RBD$_{MASCp36}$-Fab$_{B8}$-Fab$_{D14}$-mACE2 complex using ResMap[63] is shown. **c-d** Electron density maps at the interface between the RBD$_{MASCp36}$ (colored in cyan) and mACE2 (colored in purple).

Supplementary Figure 8
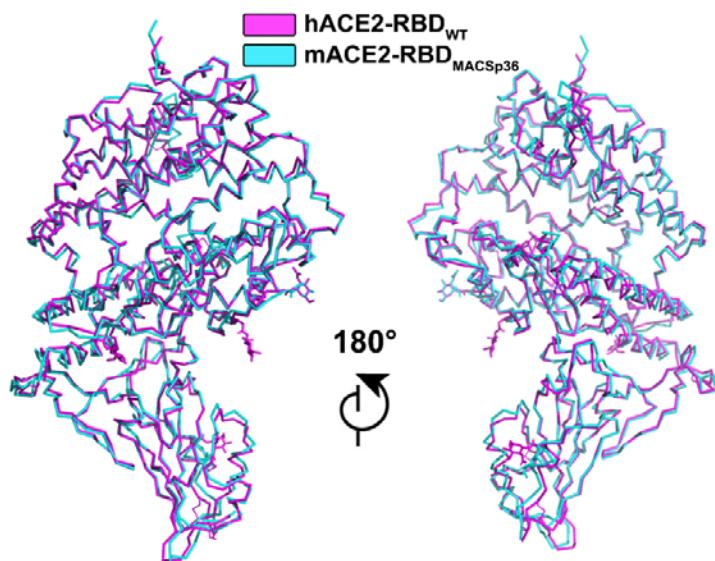
Supplementary Figure 8. Structural comparison of the mACE2-RBD$_{MACSp36}$ and hACE2-RBD$_{WT}$ complex. The mACE2-RBD$_{MACSp36}$ is shown in cyan, and the hACE2-RBD$_{WT}$ is shown in magenta.

Supplementary Figure 9
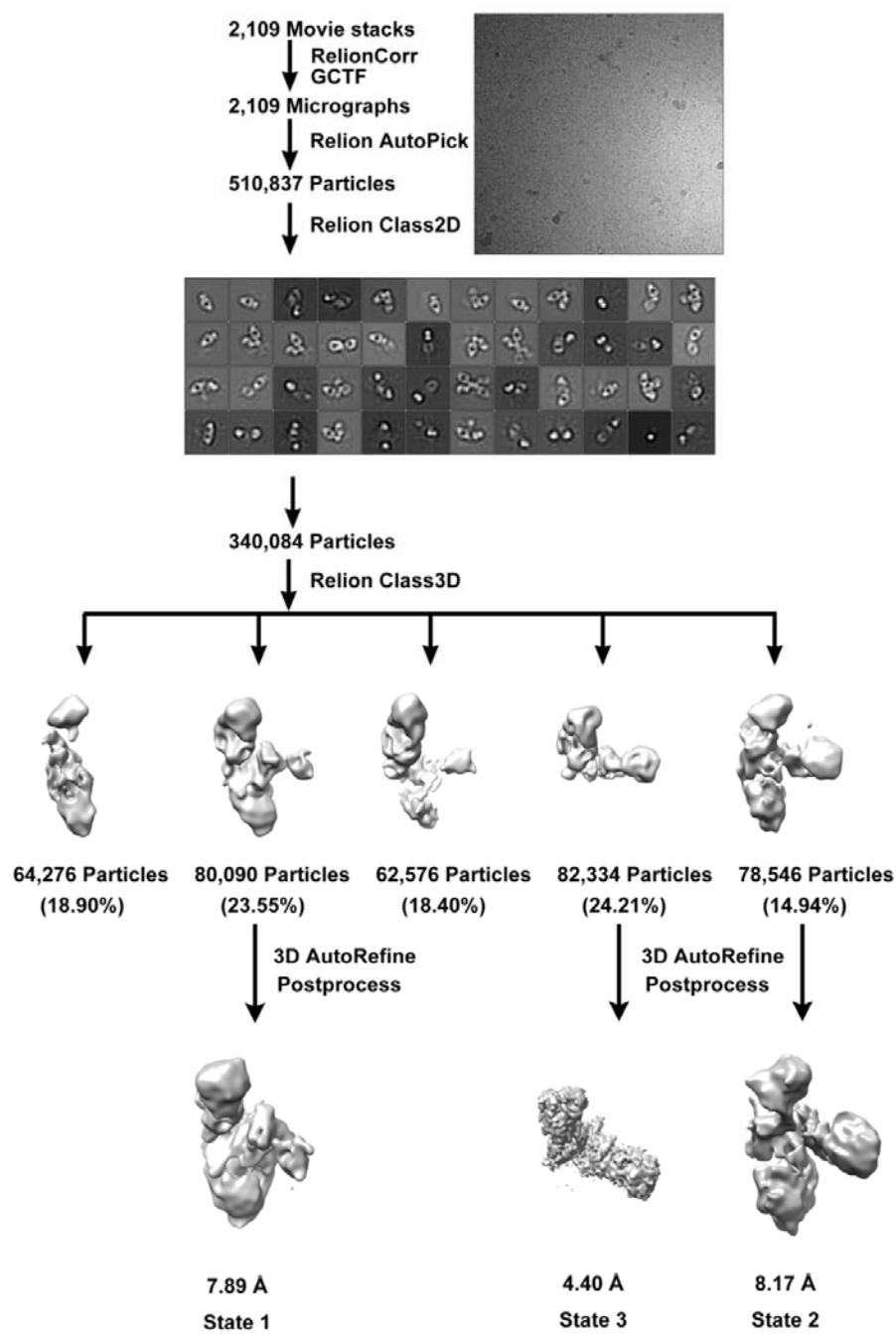
Supplementary Figure 9. Flow chart for Cryo-EM data processing of RBD$_{MASCp25}$-Fab$_{B8}$-Fab$_{D14}$-mACE2 complex.

Supplementary Figure 10
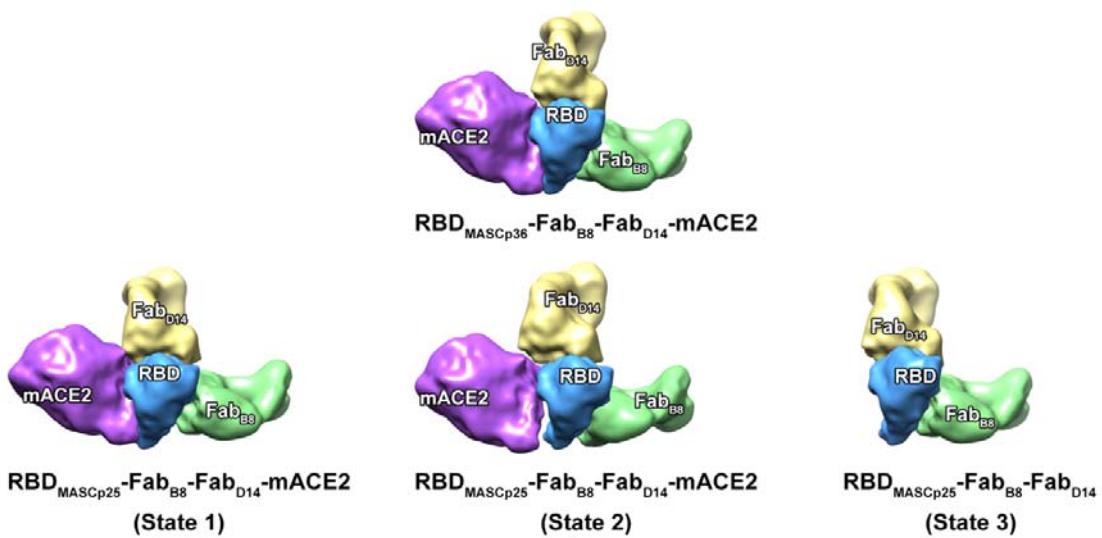
Supplementary Figure 10. Comparison of RBD$_{MASCp36}$-Fab$_{B8}$-Fab$_{D14}$-mACE2 complex with different conformations of RBD$_{MASCp25}$-Fab$_{B8}$-Fab$_{D14}$-mACE2 complex. All the subunits were filtered to a lower resolution at 15 Å. RBD mutant, mACE2, Fab$_{B8}$ and Fab$_{D14}$ are colored in blue, purple, yellow and green, respectively.

Supplementary Figure 11
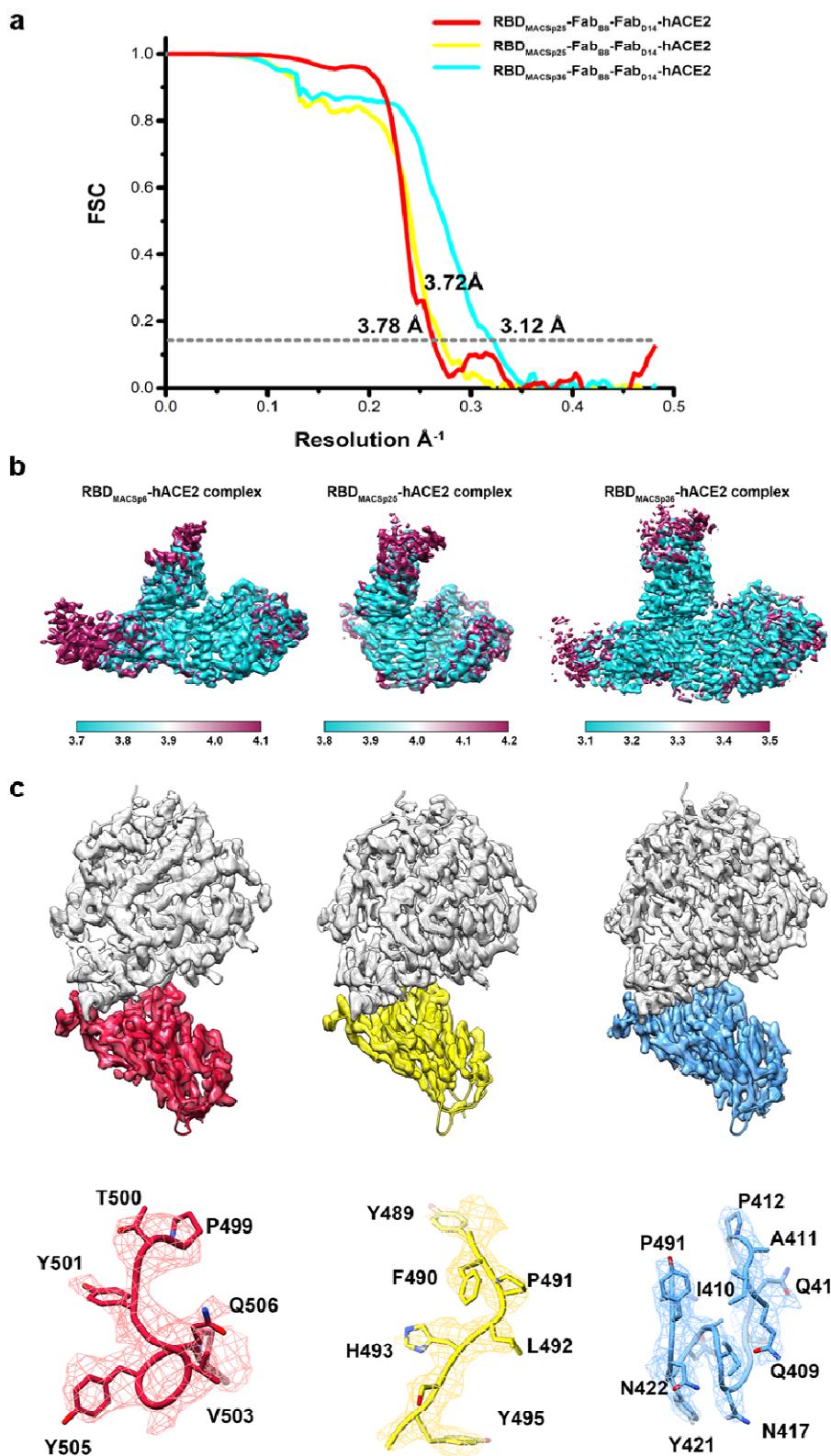
Supplementary Figure 11. Cryo-EM images and resolution evaluation of the EM maps of RBD$_{MACSp6}$/RBD$_{MACSp25}$/RBD$_{MACSp36}$-Fab$_{B8}$-Fab$_{D14}$-hACE2 complex. a. The gold-standard FSC curves of the final maps. **b.** Local resolution assessments of cryo-EM maps. Local-resolution evaluation of the maps using ResMap [63] are shown. **c.** Electron density maps at the interface between the RBD and hACE2.

Supplementary table1. Cryo-EM data collection and atomic model refinement statistics of RBD mutant-mACE2 complex

Data collection and reconstruction statistics

Protein	$RBD_{MACSp36}$-Fab_{B8}-Fab_{D14}-mACE2	$RBD_{MACSp25}$-Fab_{B8}-Fab_{D14}-mACE2 (state1)	$RBD_{MACSp25}$-Fab_{B8}-Fab_{D14}-mACE2 (state2)	$RBD_{MACSp25}$-Fab_{B8}-Fab_{D14}-mACE2 (state3)
Voltage (kV)	300	300	300	300
Detector	K2	K2	K2	K2
Pixel size (Å)	1.04	1.04	1.04	1.04
Electron dose ($e^-/Å^2$)	60	60	60	60
Defocus range (μm)	1.25-2.7	1.25-2.7	1.25-2.7	1.25-2.7
Final particles	162,615	80,090	78,546	82,334
Resolution (Å)	3.69	7.89	8.17	4.40

Models refinement and validation statistics

Ramachandran statistics				
Favored (%)	92.38			
Allowed (%)	7.43			
Outliers (%)	0.11			
Rotamer	0.09			

outliers (%)

R.m.s.d

Bond lengths (Å)   0.02

Bond angles (°)   1.26

Supplementary table2. Residues of RBD$_{MACSp36}$ interacting with mACE2 at the binding interface (d < 4 Å)

RBD$_{MACSp36}$	mACE2
Residues	
N417	N30
	Q34
L455	Q34
F456	N31
A475	T27
F486	S82
N487	N24
Y489	T27
	F28
	N31
H493	N31
	E35
G496	D38
Q498	Q42
	L45
T500	Y41
	L45
	D355
	K357
Y501	Y41
	H353
	G354
G502	H353
	G354
Y505	H353

Supplementary table3.   Cryo-EM data collection and atomic model refinement statistics of RBD mutant-hACE2 complex

Data collection and reconstruction statistics

Protein	RBD$_{MACSp6}$-Fab$_{B8}$-Fab$_{D14}$-hACE2	RBD$_{MACSp25}$-Fab$_{B8}$-Fab$_{D14}$-hACE2	RBD$_{MACSp36}$-Fab$_{B8}$-Fab$_{D14}$-hACE2
Voltage (kV)	300	300	300
Detector	K2	K2	K2
Pixel size (Å)	1.04	1.04	1.04
Electron dose (e$^-$/Å^2)	60	60	60
Defocus range (μm)	1.25-2.7	1.25-2.7	1.25-2.7
Final particles	69,324	68,211	85,978
Resolution (Å)	3.78	3.72	3.12

Models refinement and validation statistics

Ramachandran

statistics			
Favored (%)	94.65	94.98	96.7
Allowed (%)	5.34	4.99	3.30
Outliers (%)	0.00	0.00	0.00
Rotamer outliers (%)	0.01	0.03	0.00
R.m.s.d			
Bond lengths (Å)	0.01	0.02	0.01
Bond angles (°)	1.07	1.23	1.02